JGR Earth Surface

RESEARCH ARTICLE
10.1029/2018JF004872

Evolution Model for the Absheron Mud Volcano: From In Situ Observations to Numerical Modeling

Arthur Blouin[1,2,3], **Patrice Imbert**[2], **Nabil Sultan**[1], **and Jean-Paul Callot**[3]

[1]Ifremer, Géosciences Marines, LAD, Plouzané, France, [2]R&D/EP Total S.A., Pau, France, [3]E2S-UPPA, Laboratoire des Fluides Complexes et de leurs Réservoirs, IPRA, Université Pau and Pays Adour, Pau CEDEX, France

Key Points:
- The Absheron mud volcano, unlike many mud volcanoes in the South Caspian Basin, is not sourced from the deep Maykop Formation but from the Upper Productive Series
- The developed numerical model shows that an interaction between methane-saturated areas and potential rupture zones allows locating the mud volcano formation
- A formation model is proposed where hydrofracturing is the initial trigger for the subsequent gas exsolution and expansion that disaggregate and remobilize weak sedimentary layers

Correspondence to:
A. Blouin,
arthur.blouin@ifremer.fr

Citation:
Blouin, A., Imbert, P., Sultan, N., & Callot, J.-P. (2019). Evolution model for the Absheron mud volcano: From in situ observations to numerical modeling. *Journal of Geophysical Research: Earth Surface*, *124*, 766–794. https://doi.org/10.1029/2018JF004872

Received 10 SEP 2018
Accepted 18 JAN 2019
Accepted article online 15 FEB 2019
Published online 19 MAR 2019

Abstract The morphology of mud volcanoes (MVs) has been extensively studied over the last few decades. Although recent research has begun to focus on deep processes and structures, little is known about mud generation mechanisms. This study aims to investigate the feeder system and formation of an active kilometer-scale MV by relying on a 3-D seismic survey and an in situ data set on the Absheron anticline (South Caspian Basin). Seismic data show a depleted area in the Anhydritic Surakhany Formation (ASF), whose mineralogical composition fits with surface mud. Well data show that the ASF is a succession of evaporitic beds and low-temperature shales near its fracture pressure. Biostratigraphic analysis confirms a Pliocene origin for the mud, suggesting that the ASF may be the source. Numerical modeling of sedimentation coupled with laboratory test results and well sonic logs fairly reproduces the observed in situ overpressure trend. Two-dimensional methane diffusion coupled with overpressure caused by rapid sedimentation highlights the superposition of critical fracturing conditions with methane-saturated sediments at the base of the studied MV. The present study demonstrates the predominant role of fluid overpressure due to sedimentation and gas saturation in the formation of the Absheron MV, and this is shown to occur as follows: (1) methane migration through the thrust-related faults reaching the ASF, accompanied by (2) lateral overpressure, caused by rapid sedimentation, diffusing along the ASF leading to (3) hydro-fracturing of overpressured and methane-saturated sediments resulting in an important decrease in overpressure, causing (4) gas exsolution and expansion triggering sediment remobilization.

Plain Language Summary Mud volcanoes have proved to be a real risk for people living near them (e.g., Lusi catastrophe, Indonesia) and for infrastructures. While their surface morphology is well understood and their plumbing system is correctly imaged by high-resolution seismic technology, their formation mechanisms and their trigger is yet to be understood. The South Caspian Basin is known for the presence of a large number of active structures. On the Absheron anticline, a giant active mud volcano is surrounded and covered by a large data set from seismic imaging to sediment cores. From the analysis of the seismic data, and from diverse measurements on sediments, we were able to locate the source of the mud, which is shallower than the source for many mud volcanoes in the region. We developed a numerical model able to reproduce the pore pressure trends recorded at the wells, and it shows that the interaction between methane-saturated areas and potential rupture zones is able to explain the mud volcano location. Finally, based on the different results and observations, a formation model is proposed where hydrofracturing is the initial trigger for the subsequent gas exsolution and expansion that disaggregate and remobilize weak sedimentary layers.

1. Introduction

Although mud volcano (MV) surface morphologies have been described in detail and worldwide, both onshore and offshore, little is known about their evolution and formation processes (e.g., Deville, 2009; Kopf, 2002; Mazzini & Etiope, 2017). On the other hand, earlier extensive work on fluid emissions at the surface has improved understanding of subsurface processes and the multiple sourcing of the different elements forming the material ejected by MVs (Deville, 2009; Kopf, 2002; Mazzini & Etiope, 2017).

Nevertheless, recent technical improvement of geophysical tools, such as high-resolution 3-D seismic imaging, allows for detailed analysis of the MV's rooting system and has opened the way for studying mud generation processes (Dupuis, 2017; Kirkham et al., 2017a; Stewart & Davies, 2006). Understanding these generation mechanisms is a key issue for geohazard assessment (e.g., the Lusi catastrophe near

Sidoarjo, Indonesia, since 2006; Tingay et al., 2015), for environmental impacts on seabed ecosystems (Foucher et al., 2009; Zitter, 2004), targeting drilling areas, and anchoring zones for offshore infrastructures (Contet & Unterseh, 2015; M. Tingay et al., 2008). Furthermore, one characteristic shared by all MV's around the world is the presence of gas in the ejected material (Etiope et al., 2009; Hedberg, 1974). Yet it is not clear at present if the gas is a driver of mud extrusion or a passive actor, captured in the mud during its ascent. If gas has a driving role in mud extrusion, the understanding of mud generation mechanisms could provide elements to quantify the volume of expelled methane and therefore evaluate the natural contribution of MVs to the atmospheric carbon budget (Kopf, 2002).

The South Caspian Basin (SCB), along with its onshore continuation, the Lower Kura Basin, is a prolific hydrocarbon basin and is also known to hold the highest density of MVs (I. Guliyev et al., 2010; A. Mazzini & Etiope, 2017). The Absheron gas field is a challenging exploration and production area due to the presence of a giant active MV. A high-resolution 3-D seismic block was acquired in 1996, two exploration wells were drilled in 1999 and 2011, and a geotechnical campaign with sediment core sampling and in situ measurements was operated in 2014 for geohazard assessment.

Altogether, we have a rare opportunity to study a MV with a complete set of surface and subsurface data. Several issues are assessed in this article regarding the stratigraphic source of the mud, the stratigraphic and lateral location of the mud generation zone, and the physical mechanisms responsible for the MV formation.

We provide within this study a detailed geomorphological description of the structure as well as the extrusion timing based on seismic imaging and other data. Well data and sediment analysis results were integrated into numerical 1-D and 2-D models in order to quantify the lateral pressure transmission and the gas migration effect. Finally, a conceptual evolution model based on these results is proposed.

2. Regional Setting

The SCB is a remnant of the Paratethys Sea that became isolated from the world ocean during the Late Miocene, Early Pliocene, at the end of the compressive phase of the Alpine tectonic cycle (Bochud, 2011; Golonka, 2007; Popov et al., 2004). It is now delimited to the north by the Absheron peninsula and ridge, to the south by the Alborz massif, to the west by the Greater and Lesser Caucasus separated by the Kura depression, and to the east by the Kopet Dagh (Figure 1; Allen et al., 2002; Brunet et al., 2003; Popov et al., 2004; Morley et al., 2011).

Since the Middle Miocene, compression uplifted all these massifs and triggered the high-amplitude folding of the South Caspian sedimentary series (Allen et al., 2002; Egan et al., 2009; Javanshir et al., 2015; Popov et al., 2004). This compression initiated the subduction of the South Caspian basement below the basement of the North Caspian domain, creating the Absheron ridge in-between (Figure 1; Allen et al., 2002 ; Stewart & Davies, 2006). The subduction allowed the deposition of more than 8 km of sediments over the last 5.5 Myr based on a representative stratigraphic column of the northwestern part of the basin, which is faster than sedimentation rates recorded in typical foreland basins (Allen et al., 2002; Morley et al., 2011; Stewart & Davies, 2006).

The Maykop Formation was deposited from the Late Oligocene to the Early Miocene in a shallow marine anoxic environment (Golonka, 2007; Hudson et al., 2008; Popov et al., 2004). It is the main hydrocarbon source rock for the Caspian and Black Sea areas (Allen et al., 2002; Hudson et al., 2008) and acts as the main décollement level for the high-amplitude folds of the SCB (Allen et al., 2002; Stewart & Davies, 2006). The Maykop sediments are mainly organic-rich clays with a minor fraction of coarser detrital material (Hudson et al., 2008).

Post-Maykop Miocene sediments were deposited in a context of global regression until basin isolation occurred in the Late Miocene. These sediments are shallow marine and lacustrine thick clayey deposits (Allen et al., 2002; Javanshir et al., 2015).

The Pliocene was dominated by deltaic and lacustrine environments during a regression phase, fed from the ancestral Kura, Volga, and Amu-Darya rivers that drained sediments from all the topographic highs surrounding the basin (Abdullayev & Leroy, 2016; Allen et al., 2002). The subduction-related subsidence at

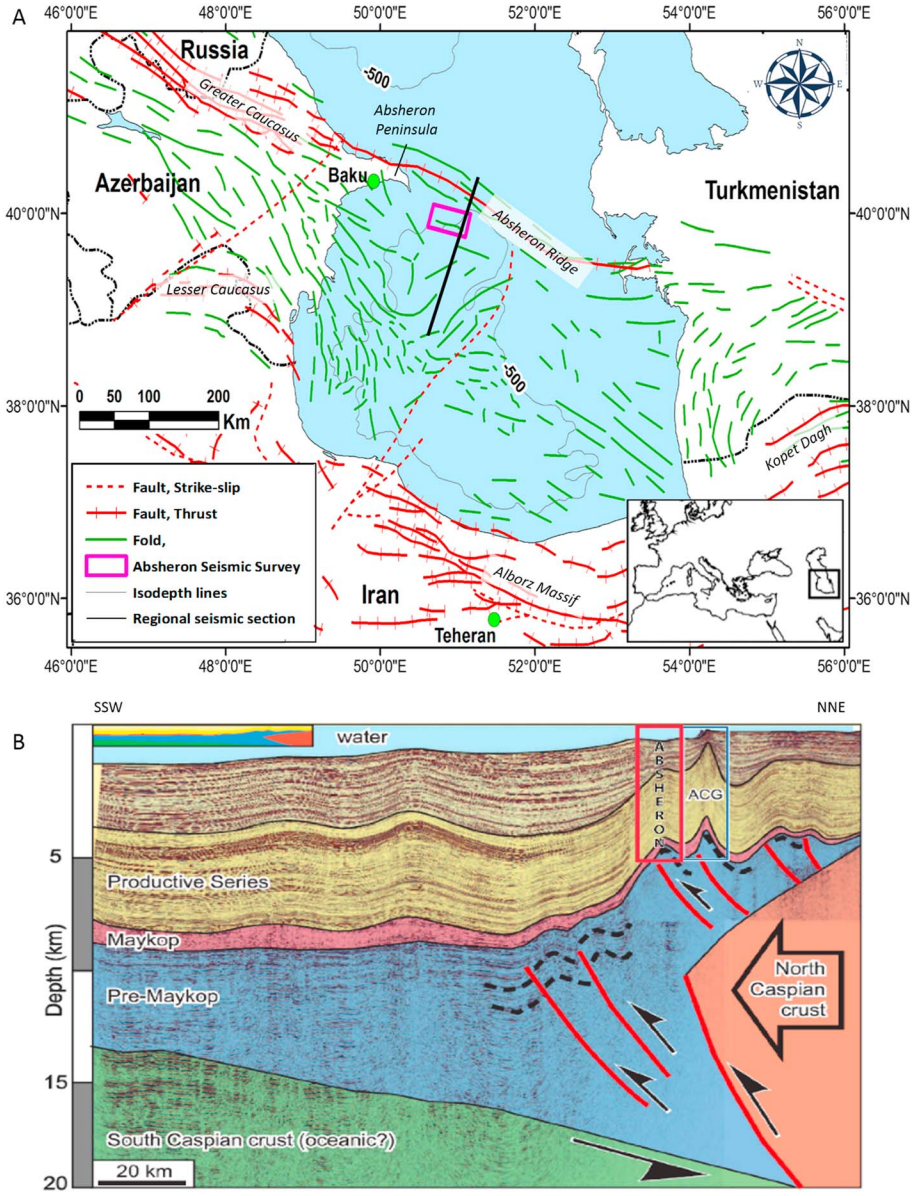

Figure 1. (a) Structural map of the South Caspian region showing the main folds and faults, structural domains, and depocenters (modified from Oppo et al., 2014). (b) Regional interpreted deep seismic section, showing the main subsurface structural elements with the folds above the Maykop detachment level associated in the northern part to deeply rooted thrusts. The location of the line is shown on the left map by a black line. The red box shows the approximate location of the Absheron structure (modified from Stewart & Davies, 2006).

the end of the Miocene accommodated the deposition of thick deltaic deposits containing the regional hydrocarbon reservoirs and forming the Productive Series (PS; Allen et al., 2002; Javanshir et al., 2015). The sedimentation rate was very high, reaching 2.4 km/Myr, allowing the deposition of up to 6 km of PS sediments (Allen et al., 2002; Brunet et al., 2003; Stewart & Davies, 2006). At the top of the Surakhany Formation (Upper PS), the regression was maximal and evaporitic beds are found in the northern part of the basin (Javanshir et al., 2015). This interval will hereafter be called Anhydritic Surakhany.

Above the PS, the Akchagyl Suite consists of open marine mudstones. This transgressive interval records the temporary reconnection of the SCB to the world ocean from 2.4 to 1.6 Ma (Allen et al., 2002; Dupuis, 2017; Javanshir et al., 2015). From 1.6 Ma to present, deepwater lacustrine and brackish conditions have dominated, forming the Absheron Suite and younger units.

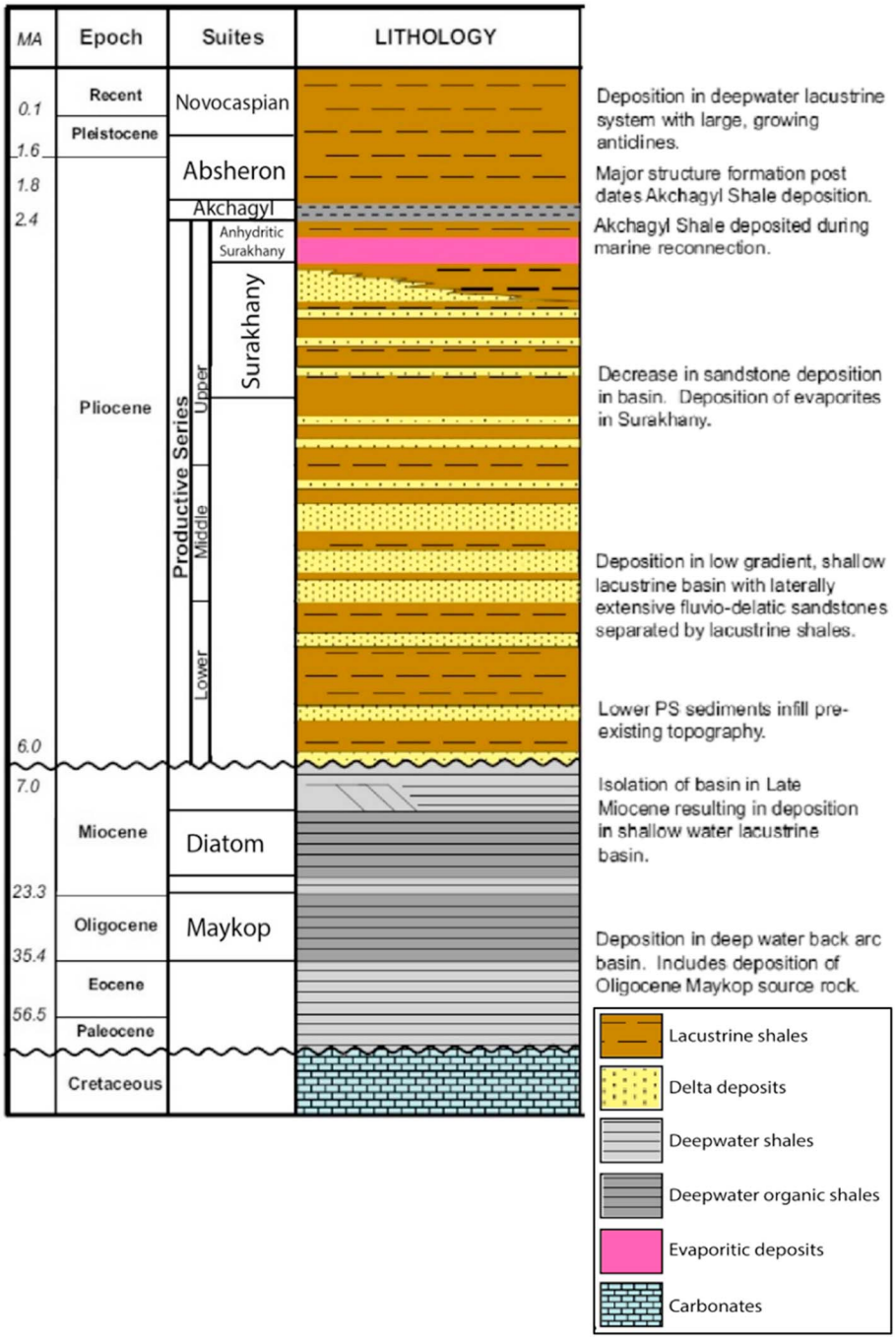

Figure 2. Stratigraphic column for the South Caspian Basin showing the ages, lithology, and main tectonic and paleo-geographical context from Cretaceous to present (modified from Javanshir et al., 2015).

Information on the stratigraphy of the SCB is synthesized in Figure 2.

The presence of the high total organic carbon Maykop Formation and of the well-connected PS reservoirs make the SCB a prolific hydrocarbon basin (Alizadeh et al., 2017; Hudson et al., 2008; Javanshir et al., 2015). The Maykop Formation generates gas in the deeper part of the basin and is still generating oil onshore and in the northern margin of the basin (Javanshir et al., 2015). Large-scale anticlines (50–150 km long), detached over the overpressured and under compacted Maykop formation (Morley et al., 2011), form excellent oil and gas traps as hydrocarbons migrate from the deep basin into the onshore

heights along the regionally continuous reservoirs (Javanshir et al., 2015). The large-scale anticline main growth stage occurred at the end of Pliocene. However, fold-growth is ongoing although slower (Mosar et al., 2010).

One hundred and eighty active MVs are listed onshore, and at least the same amount is estimated in the offshore part of the SCB (I. S. Guliyev et al., 2001; Kopf, 2002; A. Mazzini & Etiope, 2017; Milkov, 2000). These structures are mainly located along the crests of anticlines where oil and gas have accumulated in reservoirs (E. Deville, 2009; Javanshir et al., 2015; A. Mazzini & Etiope, 2017). They are generally considered to be sourced by the Maykop Formation (Kopf, 2002; Roberts et al., 2010; Stewart & Davies, 2006). Additionally, Fowler et al. (2000) noticed on the offshore Shah Deniz anticline a close relationship between the development of folds and MV activity as MVs activated during or after fold initiation and the authors correlate structural growth with MV activity phases.

The Absheron anticline is a NW-SE oriented, 40-km-long fold, located at the northwestern edge of the SCB, 100 km to the south-west of Baku and 50 km south of the ACG gas field (Figure 1a). Methane was recently discovered in the Absheron field, and a giant active MV pierces the crest of the structure at the southwestern limit creating potential hazards for drilling operations (Contet & Unterseh, 2015). Previous studies on the Absheron anticline evidenced the presence of four mass transport deposits in the Post-Absheron interval (Imbert et al., 2014). The most recent mass transport deposit covers the whole anticline with the exception of the MV location where it stumbles on the northern flank of the volcano. Morphology of the MV in the upper 500 m of the sediment pile is described in Dupuis (2017). The poorly imaged central part is surrounded by three stacked wedges affected by multiple thrusts. Recent activity of the MV is confirmed by four mudflows imaged in the first 100 m below seafloor (BSF).

3. Materials and Methods

3.1. Seismic Data

This study focuses on the Absheron anticline, where an active MV is imaged by a 3-D seismic survey (limits and location on Figure 1). The seismic survey covers 650 km^2, in water depths ranging from 180 to 700 m. The seismic sections presented here are from Kirchhoff prestack depth migration reprocessing (Robein, 2010), which was applied on 550 km^2 of the seismic survey. The velocity model used in the reprocessing aimed to improve the imaging of the deep structures (thrust and dips), taking into account the lateral velocity variations across the thrust as well as the velocity heterogeneity in the shallow intervals due to the presence of the MV and free gas (F. Adler, 12/12/2018, personal communication). The model parameterization is a vertical transverse isotropy that considers the vertical anisotropy imposed by the sedimentary strata (Robein, 2010). The model was entirely built by tomography inversion (Robein, 2010), and in the deep part, it was corrected using an interpretative method in order to preserve the structural coherency and to fit the well data (F. Adler, 12/12/2018, personal communication). The seismic volume is composed by 2,203 inlines and 2,120 crosslines with 12.5-m spacing inline and 18.5 crossline. The vertical resolution varies with depth as it depends on interval velocity. From visual observations of the sections, we estimate a resolution approximately 20 m in the strata above 2,000 m, progressively decreasing to 150 m at 11 km.

Seismic interpretation was carried out using the Total in-house software Sismage (Guillon & Keskes, 2004). From the 3-D seismic cube, we calculated the seismic coherency attribute, which can be projected on horizontal slices or seismic horizons. Seismic coherency allows to laterally differentiate continuous areas (undisturbed deposits) from low continuity zones (faults or MV deposits for instance; Bahorich & Farmer, 1995).

Each medium has its own acoustic impedance. Therefore, when a seismic signal reaches a limit between two media with different impedances, part of the acoustic signal will be reflected (Nely, 1986). A seismic signal can be decomposed in wavelets, which are characterized by their polarity, their amplitude (peak area), its period, and its phase (Nely, 1986). Normal polarity is given by the seafloor polarity, which in the data presented hereafter are a wavelet with a strong central positive amplitude surrounded by two weak negative amplitudes. Thus, the normal polarity is a strong positive peak enclosed between two weak negative peaks indicating a stepwise increase in impedance. The opposite shows a stepwise decrease in impedance (Nely, 1986; Ricker, 1953).

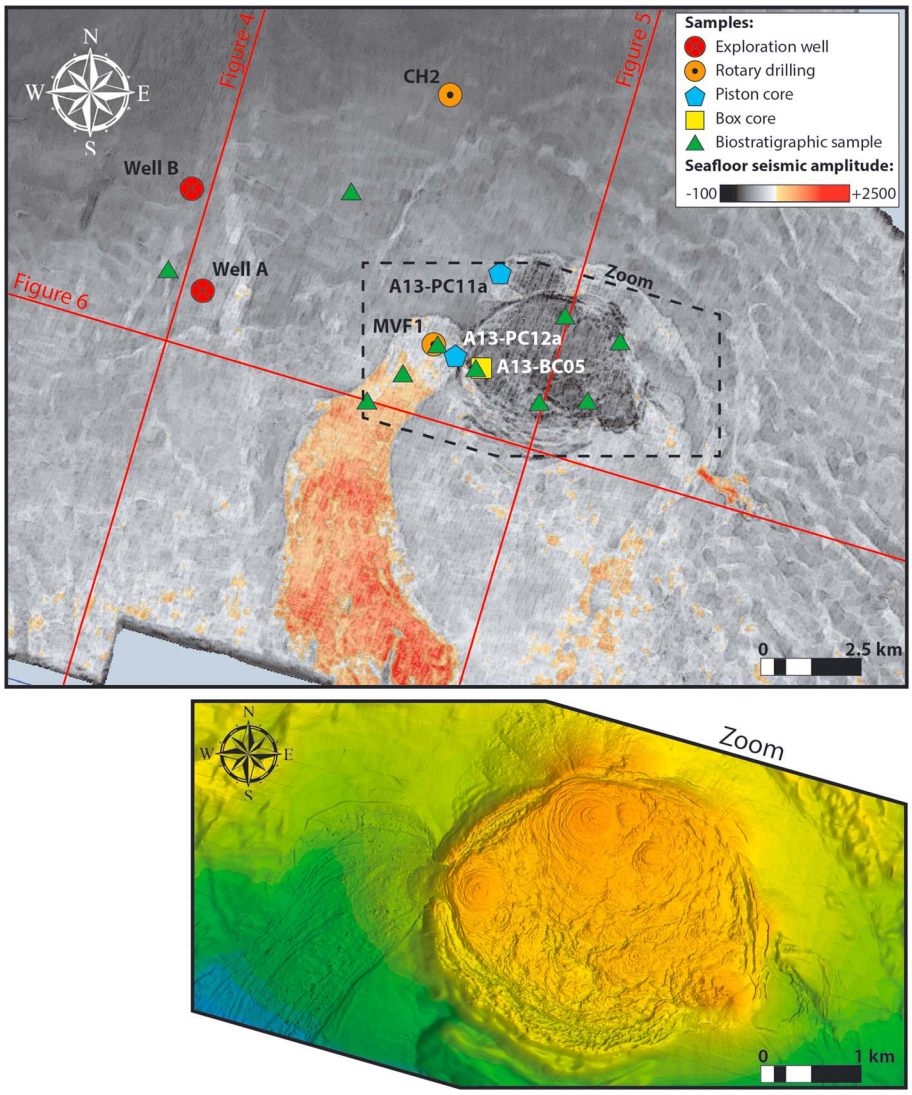

Figure 3. Seismic amplitude map of the seafloor around the Absheron mud volcano. In orange, a high-amplitude mud-flow is imaged to the west of the volcano. The dark patch corresponds to the shield composing the mud volcano itself. On the same map, the location of the different coring and drilling sites are shown. Limits and location of the 3-D seismic survey are presented on the regional map of the South Caspian Basin (SCB; Figure 1a). The red lines indicate the location of the seismic lines presented in Figures 4 to 6. The dotted black polygone is the limit of the zoom shown below, presenting a detailed image of the seafloor on and around the mud volcano acquired with a multibeam echo sounder. Orange stands for the shallower areas; green is for the deeper parts.

The presence of free gas is a well-documented cause of attenuation or data wipe-out (Benjamin & Huuse, 2017; Graue, 2000). MVs are known to be accompanied by large emissions of gas (Kopf, 2002; A. Mazzini & Etiope, 2017). Therefore, seismic masking is expected to occur below large structures such as the Absheron MV (AMV; Benjamin & Huuse, 2017; Graue, 2000). Imaging issues that cannot be settled by migration algorithms may arise from steep dips (Day-Stirrat et al., 2010).

Horizons were propagated and named according to stratigraphic limits encountered in the two exploration wells drilled on the Absheron anticline (Figure 3 for location). These stratigraphic limits are interpreted based on cuttings analysis and gamma ray, sonic, and resistivity logs.

In parallel of the seismic imaging, high-resolution bathymetric maps (Figure 3) were acquired using a multibeam echosounder.

3.2. Sediment Cores and Geotechnical Analysis

3.2.1. Sample Collection

A marine geological and geotechnical survey of the seabed above the Absheron gas discovery was carried out in 2014 in order to better constrain and delineate geological hazards associated with the MV (Total proprietary report, G. Dan & S. Po, 12/09/2017, personal communication). The geotechnical/geological survey used rotary drilling, AUV (autonomous underwater vehicle) sampling with box corer and piston corer, and in situ geotechnical testing (Cone Penetration Testing [CPT]). Well logging and CPT were performed on two boreholes: CH2 was located outside the MV area to provide a stratigraphic reference in continuous series, and MVF1 sampled on a MV flow (for location see Figure 3).

To improve the characterization of MV deposits, we selected eight samples from different sediment cores. Table 1 lists the coordinates and depth below seabed of these samples, and Figure 3 shows their location with respect to the MV. The samples were selected to provide information on the spatial and temporal variability of the MV deposit (Total proprietary report, G. Dan & S. Po, 12/09/2017, personal communication). Five samples were selected at three different depths from the same rotary drilling cores MVF1, thus potentially sampling different mud eruption episodes. One sample from A13-PC12a core was taken from the same mudflow as the one drilled by MVF1 but at a different location. A different mudflow was sampled on the A13-PC11a core at the northern edge of the MV. Finally, a sample was taken from the A13-BC05 core directly on the top of the mud shield (see Table 1 for further details and Figure 3 for location).

3.2.2. Mineralogical and Biostratigraphic Analysis of Mud

The MVF1E RAW sample was separated into two different grain size classes, with a limit at 5 μm, in order to compare the composition of the clay-size fraction and the coarser fraction. The >5 μm of the raw sample was extracted by suspension of fine fractions in water followed by centrifugation.

Eight samples were analyzed using a reference quantitative mineralogy method called MinEval QM (Table 1; Fialips et al., 2018). This method is based on the integration of results from various measurements performed on crushed samples, including X-ray diffraction on bulk powders and extracted fine fractions, loss on ignition, X-ray fluorescence, insoluble residue upon HCl 15% treatment, bulk solid density, and cationic exchange capacity (see Fialips et al., 2018 for more details). This method performs an initial semiquantitative mineralogy analysis by Rietveld refinement of the X-ray diffraction patterns (Rietveld, 1969), and quantification is completed applying a dedicated software that uses an iterative approach. The <5-μm fraction of MVF1E-RAW only obtained a semiquantitative mineralogical analysis of clay minerals. The quantity of fine material obtained after separation was insufficient to perform the complete quantitative study.

Furthermore, a biostratigraphic study by Chevron in 2000 was carried out with the aim of dating the oldest material composing the mudflows. A series of samples were recovered in and around the volcano location (green triangles in Figure 3). The samples around the structure were used as age control points. The elements picked and counted on the different samples are diatoms, pollens, foraminifera, nannofossils, and ostracods.

Initial grain size distribution for the natural mud was determined using the Mastersizer 3000 device for laser diffraction granulometry (Ryzak & Bieganowski, 2011).

3.2.3. Geotechnical Analysis of Mud

Oedometer tests with permeability measurements were carried out on four samples taken from the GT1-MVF1 core (MECA 6-10-15-22 in Table 1 and tests from 1 to 8 in Table 2). Tests were duplicated in order to check for potential trial mistakes. The samples were selected based on CPT (Das, 2013) data showing at least four mechanically distinct intervals (Total proprietary report, G. Dan & S. Po, 12/09/2017, personal communication). The aim of these oedometer tests was to define compressibility characteristics (void ratio versus effective stress) and to determine the relationship between hydraulic conductivity and void ratio of the considered sediment intervals (ASTM International, 1996).

The void ratio e changes are tied to the vertical effective stress σ'_v by the following compressibility relation:

$$e = e_0 - \lambda \ln\left(\frac{\sigma'_v}{\sigma'_{v0}}\right) \quad (1)$$

where e_0 is the initial void ratio for a reference vertical effective stress σ'_{v0} and λ is the compression index depending on the sediments. e_0 and λ for the tested samples are shown in Table 2.

Table 1
DRX and Mechanical Sample Names and Details Used in This Study

Core name	Sample name	Type of sample	Type of analysis	Water depth (m)	Depth below seafloor (m)	
					Top	Bottom
MVF1C	DRX1	Core Sample	Mineralogy	521	3.53	3.55
	MECA-6	Core Sample	Granulometry, oedometer		3.71	3.80
	MECA-10	Core Sample	Granulometry, oedometer		5.14	5.22
MVF1D	MECA-15	Core Sample	Granulometry, oedometer	522	10.00	10.08
	MECA-16	Core Sample	Oedometer		10.41	10.48
	MECA-17	Core Sample	Oedometer		10.68	10.75
	DRX2	Core Sample	Mineralogy		19.00	19.06
MVF1E	DRX3	Core Sample	Mineralogy	522	33.04	33.06
	MECA-22	Core Sample	Granulometry, oedometer		33.08	33.15
	RAW>5 μm	fraction >5 μm	Mineralogy		34.00	34.61
	RAW<5 μm	fraction <5 μm	Mineralogy		34.00	34.61
A13-PC11A	DRX4	Core Sample	Mineralogy	467	0.91	1.00
A13-PC12A	DRX5	Core Sample	Mineralogy	505	0.11	0.17
A13-BC05	DRX6	Core Sample	Mineralogy	453	0.32	0.36

Note. Total proprietary report, G. Dan and S. Po (12/09/2017, personal communication).

The permeability relation to void ratio is assumed to be

$$\ln(K) = ae + b \tag{2}$$

with K the Darcy permeability (Das, 2013) or hydraulic conductivity (m/s), a and b are constants characteristic of the tested sediments.

The samples were all reconstituted with an artificial initial water content of around 1.5 wL (wL being the liquid limit). The wL (Table 2) was determined using the fall cone method (Feng, 2005). Oedometer tests were conducted using incremental loading according to the ASTM D-2435 method (ASTM International, 1996). The determination of hydraulic conductivities and permeability coefficients was also possible using the falling head method (Das, 2013). Using an exponential regression on the obtained measurements is necessary to obtain a law of the form of equation (2).

In order to artificially characterize the impact of coarse material on mechanical properties, additional oedometer tests were carried out on combined MECA-16 and MECA-17 samples (Tables 1 and 2) mixed with a known mass of fine sand (80–125 μm); the goal was to obtain their compressibility and permeability in order to integrate these results in the numerical diffusion model. The fractions of coarse material added to the samples were selected based on the net to gross (ratio between sand layer cumulated thickness over total interval thickness) values calculated from well data.

Table 2
Details on Sample Preparation for Oedometer Rests and Results

Test number	Sample	σ'_{vmax} (kPa)	wL	e_0	λ	Sample preparation
1	MECA-6	1765.12	0.42	1.95	0.35	1.5 wL water input
2	MECA-22	1765.12	0.43	1.7	0.34	1.5 wL water input
3	MECA-10	1765.12	0.56	2.11	0.42	1.5 wL water input
4	MECA-15	1765.12	0.44	1.79	0.32	1.5 wL water input
5	MECA-6	1765.12	0.42	2.23	0.36	1.5 wL water input
6	MECA-22	1765.12	0.43	1.9	0.33	1.5 wL water input
7	MECA-10	1765.12	0.56	2.58	0.46	1.5 wL water input
8	MECA-15	1765.12	0.44	2.18	0.34	1.5 wL water input
9	MECA-16 + 17 + 5% sand	1765.12	0.44	1.38	0.25	1.5 wL water input, mixed samples
10	MECA-16 + 17 + 10% sand	1765.12	0.44	1.23	0.23	1.5 wL water input, mixed samples
11	MECA-16 + 17 + 25% sand	1765.12	0.44	1.14	0.20	1.5 wL water input, mixed samples

3.3. In Situ Well Data and Hydraulic Conductivity Calculations

Stratigraphic information was obtained from the two exploration wells drilled on the Absheron anticline (Figure 3). Well A reached 6,506-m TVD/MSL (true vertical depth below mean sea level), while Well B reached 6,823 TVD/MSL.

Lithology is obtained from cuttings analysis. Pore pressures in shales were estimated from sonic data using Eaton's (1975) method. Sonic logs were acquired either with wireline or logging while drilling tools depending on the interval. The StethoScope pressure-while-drilling tool (Schlumberger) was used to measure in situ reservoir pore pressure. Fracturing pressure log is evaluated from leak-off tests or formation integrity tests (Lin et al., 2008), as well as downhole mud losses. Wireline tools measured temperatures at different points either in open hole or cased hole.

The sonic measurements are given as slowness of the acoustic waves, for example, the inverse of acoustic velocity. Wyllie et al. (1958) gave a relationship between measured velocity of a porous media and its porosity ϕ:

$$\frac{1}{V_m} = \frac{\phi}{V_f} + \frac{(1-\phi)}{V_s} \tag{3}$$

with V_m indicating the measured acoustic velocity, V_f indicating the acoustic velocity in pore fluid, and V_s indicating the acoustic velocity in the rock matrix.

As void ratio and porosity are linked through the relation:

$$e = \frac{\phi}{1-\phi} \tag{4}$$

it is possible to calculate hydraulic conductivities K for reservoir layers using the Kozeny-Carman relationship (Ren et al., 2016):

$$K = C_F \frac{1}{S_s^2} \frac{\gamma_f}{\mu \rho_s^2} \frac{e^3}{(1+e)} \tag{5}$$

where C_F is a shape constant around 0.2, S_s is the specific surface area of particles (m^2/g) taken here as equal to 0.5 m^2/g, γ_f is the unit weight of pore fluid (N/m^3), ρ_s (kg/m^3) is particle density, and μ is fluid viscosity ($N\ s/m^2$).

Therefore, it is possible to estimate the hydraulic conductivity of reservoirs directly from acoustic log data. Oedometer test results on natural mud allowed calculation of permeability in the shales. From the lithological log, the column was split into reservoirs and shale intervals. Using equations (2), (3), and (5), we calculate for each defined interval the hydraulic conductivity K. The net to gross ratio (cumulated sand thickness divided by total interval thickness) was calculated for each drilled formation. The arithmetic average of hydraulic conductivities gives the horizontal hydraulic conductivity for the considered formation, while the harmonic average gives its vertical hydraulic conductivity (Das, 2013).

3.4. Numerical Modeling: Sedimentation, Transient Pore Pressure, and Gas Diffusion

3.4.1. 1-D Sedimentation and Pore Pressure Accumulation

Geological formations remain at hydrostatic pressure after deposition and burial as long as pore fluids are able to escape up through the overburden or laterally toward the seabed or surface. High permeabilities or low sedimentation rates help pore water escaping during consolidation. In contrast, when permeability is low or sedimentation rate is high enough, fluids cannot escape fast enough to keep hydrostatic conditions. As loading increases through sedimentation, pore water starts to support part of the overburden pressure, which prevents pores from closing. Thus, normal consolidation is delayed, sediments become undercompacted, and pore pressure increases above hydrostatic conditions. This excess pore pressure is called overpressure and this mechanism of overpressure buildup is called compaction disequilibrium (Osborne & Swarbrick, 1997; Sultan et al., 2004; Swarbrick et al., 2002).

In this work, we calculate in one dimension the overpressure generated (Δu) only by sedimentation effect in the southern part of the considered section where the sedimentary column is the thickest. The high

sedimentation rates observed in the basin are within the strongest recorded worldwide (Allen et al., 2002; Brunet et al., 2003; Stewart & Davies, 2006). Moreover, high sedimentation rates are considered to be one of the main overpressure generation mechanism (Osborne & Swarbrick, 1997; Swarbrick et al., 2002). Therefore, the modeling work focuses on this sedimentation effect as a first approach. The SeCoV3 proprietary software of IFREMER (Sultan et al., 2004) allows quantification of the evolution of pore pressure using a back analysis based on sedimentation rates, compressibility properties (equation (1)) and permeability evolution with void ratio (equation (2)). In addition to the equations solved by SeCoV3, in the present work we use a mesh-update method considering the compressibility of sediments and the mobile position of the upper boundary (seawater-sediment interface) at each calculation step.

Sedimentation rates and the model geometry used in this study were calculated using present thicknesses and ages from Green et al. (2009). These sedimentation rates have been corrected (decompression) for compaction using Terzaghi compaction equations (Terzaghi, 1943). At the end of sedimentation and compaction modeling, we applied a trial and error method until the model matched present-day observed thicknesses.

Compressibility and permeability properties characterizing each of the defined layers were determined based on oedometer and permeability tests (Table 2) carried out on natural mud mixed with known fractions of very fine sand (ASTM International, 1996). The fractions of added sand were selected thanks to net to gross values calculated from well data (Table 3). The purpose was to model the behavior of layers having different amounts of coarser material.

3.4.2. Two-Dimensional Transient-Diffusion Process: Darcy's and Fick's Laws

The two-dimensional transient dissipation of excess pore pressure generated by the sedimentation process is considered along a 63-km-long and 10-km-thick block of the section presented in Figure 11 of Green et al. (2009). We defined the geometrical model with 300 horizontal and 50 vertical nodes by considering six stratigraphic layers, the fault network around the Absheron fold, and normal faults at the extrados of the fold.

The excess pore pressure generated by sedimentation and calculated using SeCoV3 was considered as a boundary condition for the 2-D Darcy transient flow calculation. The two-dimensional dissipation and transmission of overpressure is calculated using the 2-D diffusion equation given by

$$\frac{\partial \Delta u}{\partial t} = \left(\frac{\partial (D_{hx} \partial \Delta u)}{\partial x^2} + \frac{\partial \left(D_{hy} \partial \Delta u\right)}{\partial y^2} \right) \tag{6}$$

with Δu being the overpressure and D_{hx} and D_{hy}, respectively, the horizontal and vertical hydraulic diffusivities that are calculated directly from the horizontal and vertical hydraulic conductivities Kx and Ky (Table 3).

In addition to the transmission/diffusion of pore pressure, we considered in the present work the molecular diffusion of dissolved methane. Methane diffusion is calculated using a two-dimensional diffusion equation referred to as Fick's law (equation (7)), which allows for the description of diffusion of dissolved molecules into a solvent (Crank, 1975):

$$\frac{\partial C}{\partial t} = D_C \left(\frac{\partial (D_C \partial C)}{\partial x^2} + \frac{\partial (D_C \partial C)}{\partial x^2} \right) \tag{7}$$

with C being the dissolved methane concentration and D_C being the methane molecular diffusivity of the porous water. The effect of tortuosity of pores on molecular diffusivity is considered through the porosity of the sediment as described by Boudreau (1996).

To solve numerically the 2-D diffusion equations (equations (6) and (7)), a centered explicit finite difference discretization scheme is used by considering the initial and boundary conditions for pore pressure and methane concentration.

Faults are characterized by their own methane molecular diffusivities creating preferential pathways for methane. Moreover, as the modeled stratigraphic column is formed by a succession of metric-scale sand layers and plurimetric shale intervals, a ratio between horizontal and vertical hydraulic conductivities was integrated based on the results of the hydraulic conductivity calculations at wells (Table 3). This ratio allows modeling of the natural anisotropy of the sedimentary column due to sand-shale successions.

Table 3
Results of Hydraulic Conductivity Calculations Based on Sonic-Log Data and Oedometer Tests on Natural Mud

Layer name	Layer number in model	NTG (%)	Mean void ratio from logs	*Kh* (m/s)	*Kv* (m/s)	*Kh*/*Kv*	Void ratio ranges from 1-D model	*K* ranges from oedometer tests (m/s)	Model *kx*/*ky*
Novocaspian-Absheron	Layer 5	5	0.33	5.03E−07	2.27E−10	2212	2.73–0.36	5.01E−07 to 3.53E−10	2200
Surakhany	Layer 4	8	0.18	3.18E−09	2.13E−10	15	0.43–0.24	7.50E−10 to 4.17E−10	15
Sabunchy	Layer 3	12	0.14	1.27E−09	1.95E−10	6	0.22–0.21	4.70E−10 to 4.56E−10	6
Balakhany-Fasila	Layer 2	24	0.17	5.16E−10	2.57E−10	2	0.27–0.24	7.78E−10 to 7.05E−10	2
NKG	Layer 1	8	0.17	2.18E−10	2.10E−10	1	0.24–0.22	4.17E−10 to 3.92E−10	1

Note. NTG is the net to gross, being the ratio between total sand thickness over total interval thickness. The mean void ratio is calculated from the sonic log (equation (3)) and *Kh* (horizontal hydraulic conductivity) and *Kv* (vertical hydraulic conductivity) result respectively from arithmetic and harmonic average of calculated hydraulic conductivities on individual sand or shale layers using equation (5). The 1-D-sedimentation model gives a range of void ratio for each stratigraphic interval, corresponding to hydraulic conductivity ranges on oedometer test results obtained for different sand fraction content (Table 2). Measured and calculated *K's* are in the same ranges of magnitude.

3.4.3. Hydrofracturing

In some cases, excess pore pressure can exceed the effective least principal stress plus the tensile strength of the medium allowing hydrofracturing to occur (Alfaro & Wong, 2001). When sediments are only submitted to the load of the overlying sedimentary cover, the greatest effective stress is vertical (σ'_v), whereas the least effective stress is horizontal (σ'_h; Sibson, 2003). Fractures then open in the direction of the least principal stress and propagate in the direction of the plane perpendicular to the least principal stress (Hubbert & Willis, 1957). Therefore, in the case of sole loading effects, hydrofractures will propagate vertically.

The vertical effective stress and excess pore pressure are an output of 2-D Darcy's diffusion equation. The ratio between fracturing pressure and overburden pressure (lithostatic stress) observed in the well ranges between 0.83 and 0.99, with an average of 0.9. Consequently, we consider in the present work that hydrofracturing will occur whenever the ratio between excess pore pressure and vertical effective stress ($\Delta u/\sigma'_v$) exceeds 0.9.

4. Results

4.1. Geomorphological Investigation of the AMV

Figures 4 and 5 present two parallel SSW-NNE sections. Figure 4 runs across the axis of the Absheron fold in the vicinity of the two exploration wells drilled on the anticline and Figure 5 cuts through the center of the AMV as located on Figure 3. The ages of five of the seismic horizons that are presented in this study were calibrated from the stratigraphic results of the well (total proprietary data). We were able to map the top of Absheron Suite, the top of the Akchagyl Suite, the top of the PS, the top of the Anhydritic Surakhany Formation (ASF), the Top Diatom Suite, and the top of the Maykop Suite (see Figure 2 for the stratigraphic column). Seven other seismic horizons were interpreted in order to highlight particular structures such as normal faults or the morphology of the fold.

The deep part of the Absheron fold is cut by a deep E-W trending thrust that dies out in the Diatom Suite. This thrust has more than 2 km of throw, and the northern block overrides the southern block. The thickening of the interval between Top Diatom and Top Maykop is interpreted as the result of a backthrust system that would have been inverted later during its history. Another thrust 5 km to the NNW has a throw of only 1 km (Figure 4). The main thrust is responsible for the formation of the Absheron fold, and several folding phases can be distinguished. The PS interval has a rather uniform thickness of 5 km across the anticline with only 10% of total thinning from the flanks to the crest of the anticline, indicating a rapid deposition during a phase of low-activity for the fold (Figure 4). The Akchagyl Suite presents a thickening toward the southern flank of the fold of 300 m, corresponding to 60% of its maximum thickness (Figure 4), thus indicating that growth of the anticline was accelerated during deposition of this interval. Fold activity was still strong during deposition of the Absheron Suite as the thinning at the crest reaches 650 m for this interval, 35% of its maximum thickness. More precisely, the interval between horizons A3 and A2 recorded a thinning of 330 m (45% of maximum thickness), and between A1 and A2, 190 m (40% of maximum thickness; Figure 4). More

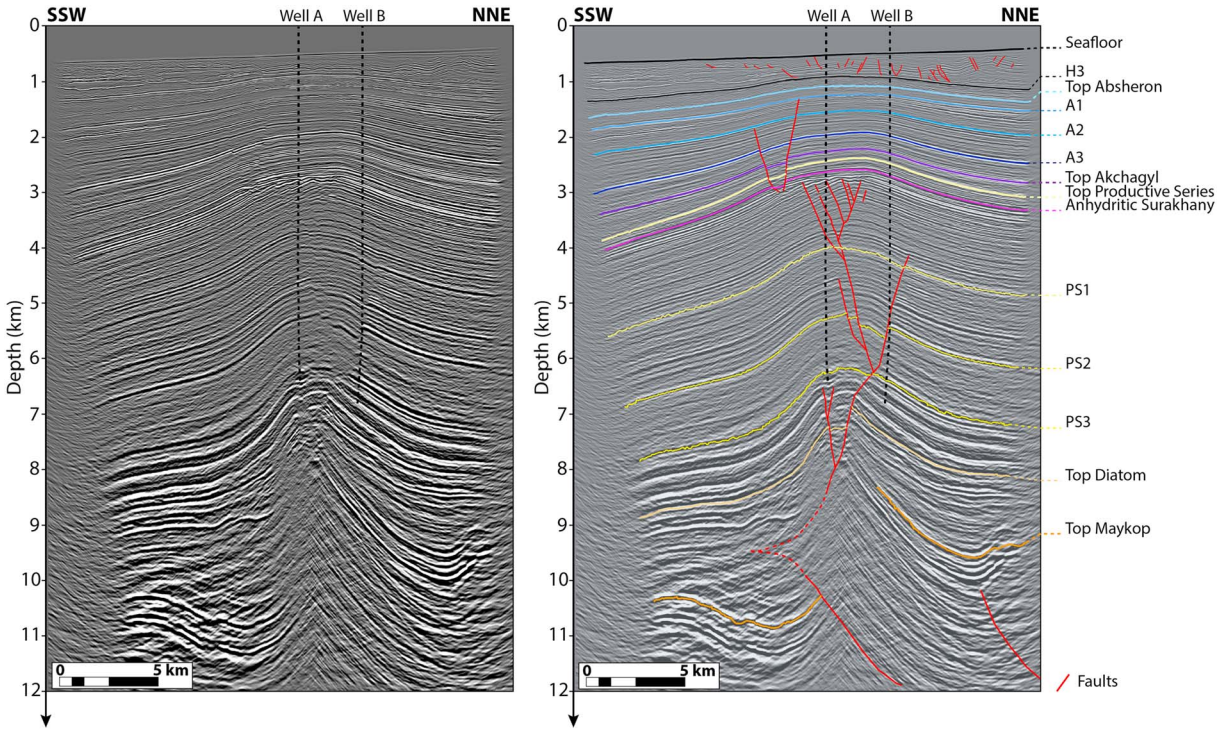

Figure 4. Uninterpreted and interpreted seismic line crossing the anticline near the two exploration wells A and B; it was used as reference for horizon picking for this study. A deep thrust cores the Absheron anticline, and another thrust, smaller, is also visible at the NNE of the section. From the thickness differences between the flanks and the crest of the structure, we note that folding started during the Akchagyl deposition. The main growing phases are during deposition of the Absheron Suite (A3-A1) and later during the Post-Absheron times. See Figure 3 for location.

recently, during Post-Absheron times, the fold reactivated and another 450 m of thinning (45% of maximum thickness) is visible from Top Absheron horizon to the seafloor (Figure 4). Therefore, sediment thinning at the crest of the anticline indicates that fold activity really started at the Akchagyl times, when it reached its climax. During the Absheron Suite deposition, the fold activity was intense for a longer time interval, and recent intense fold activity was also recorded in the Post Absheron interval.

Besides, normal faults on the extrados of the fold form a complex network from the thrust up to the Upper PS (Figure 4). The backthrust was then inverted to form the main observed normal fault.

The AMV is located in the SE part of the 3-D seismic survey. Figure 3 shows the seismic amplitude of the seafloor horizon, with a color-scale set to outline high and low amplitude zones. Orange stands for the highest amplitude and darker areas correspond to lower amplitude zones. The high-resolution bathymetric map (Figure 3) reveals present seafloor morphology related to recent MV activity. Near-surface morphology of the MV was already detailed by Dupuis (2017), with the presence of three main wedges (*Transparent Facies* and *Chaotic Facies* on Figure 5) and at least four recent mudflows evidenced on seismic data.

This MV is a subcircular mud shield, 4 to 5 km in diameter (Figure 3). It is surrounded by a gently dipping apron (average outward slope from 4 to 6°); the relief above the surrounding seafloor does not exceed 70 m (Figure 3). The highest area is a relatively flat plateau, but at a closer look reveals at least four gently mounded circular structures, 0.5- to 1-km diameter (Figure 3); we interpret these as the loci of most recent mud emission. At the western edge of the mud shield, a 12-km-long, 1.5- to 3-km-wide high-amplitude patch extends from the volcano to the west before following the natural slope toward the south of the Absheron seismic survey (Figure 3). This high-amplitude patch was already described as a giant mudflow by Dupuis (2017). This mudflow shows up strongly on seabed amplitude maps, indicating that is closer to seabed than the resolution of the data set.

Interpretation of the section running through the center of the AMV (Figure 3 for location) is given in Figure 5. The first obvious observation is the presence of a large seismically transparent body spreading horizontally in the first 500 m BSF. Four wedges of this feature are imaged at the SSW from the center of the

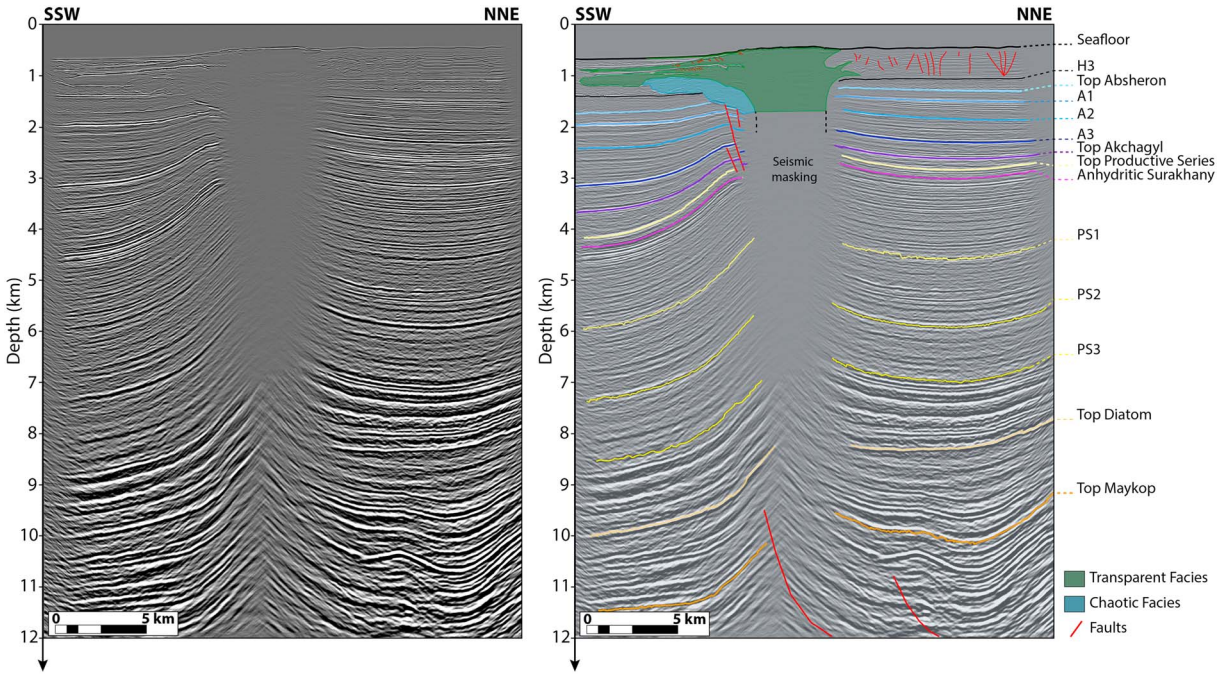

Figure 5. Uninterpreted and interpreted seismic line across the active mud volcano. The first 2 km are clearly imaged and show four seismically transparent wedges, corresponding to mudflows. A chaotic signal below can be discriminated from the blind signal and is interpreted as reworked sediments. The rooting system is blind, maybe due to a masking effect from the low velocity mud deposits. Near the blind area, some normal faults are present between 1.5 and 3 km. A deep thrust is coring the main anticline. The activation of the mud volcano is contemporaneous to the main folding phase (see text and Figure 4 for details and Figure 3 for location).

volcano. These interdigitations reunite at the center of the structure and form one large seismically transparent zone from the seafloor down to 1 km BSF. The shallowest digitation follows exactly the seafloor seismic horizon and is less than 50 m thick. As it was sampled notably with the box core A13-BC05 (Figure 3), this transparent area can directly be interpreted as mudflow deposits forming the MV edifice (green patch on Figure 5). Below 2 km at the center of the structure, a seismically transparent cone goes down to 7 km. This area could reveal the masking effect of the low velocity mass formed by the shallower mud deposits that may also be saturated with gas, preventing the acoustic signal from propagating below. Another seismic facies can be discriminated from the blind signal: the blue patch can be described as a chaotic signal. This area is located between the mudflows and host sediments.

Moreover, the deeply rooted thrusts described on Figure 4, are still imaged, yet not as clearly because of the seismic masking. Nevertheless, the AMV is centered above the exact vertical of the main thrust (Figure 5). The first mudflows imaged were deposited during the post-Absheron interval, between seismic horizons H3 and the Seafloor. No activity is recorded before H3. Consequently, the AMV seems to have been initiated after the end of the Absheron folding phase, during the post-Absheron folding phase.

Normal faults are imaged near the blind cone (Figure 5). They cross the Absheron Suite and end in the Upper PS, near the Anhydritic Surakhany interval.

After the time of extrusion, we addressed the issue of the primary source of the mud by identifying a possible depletion zone (Kirkham et al., 2017b; Stewart & Davies, 2006). In order to alleviate the seismic masking, we looked at lines crossing the volcano away from its center. Figure 6 presents a WNW-ESE seismic section, perpendicular to the section shown in Figure 5 and crossing the volcano 2 km away from its center. The section crosses the distal part of both transparent facies bodies and of the chaotic facies body from 0.5 to 2 km. The mudflow deposits appear 200 m above the H3 seismic horizon. The Top Absheron horizon is truncated by the chaotic mass. Deeper seismic horizons, from Absheron to Top PS, bend downwards, forming a bowl shape particularly visible on tracked horizons A1 and A3. The Anhydritic Surakhany horizon and the 200-m-thick interval below are truncated by downlapping younger intervals. Another truncated interval, 400 m thick, is imaged between 3,400 and 3,800 m and contained approximately the lower interval of the Upper PS, below the ASF. From 3,800 m to deeper, horizons become continuous and flat again.

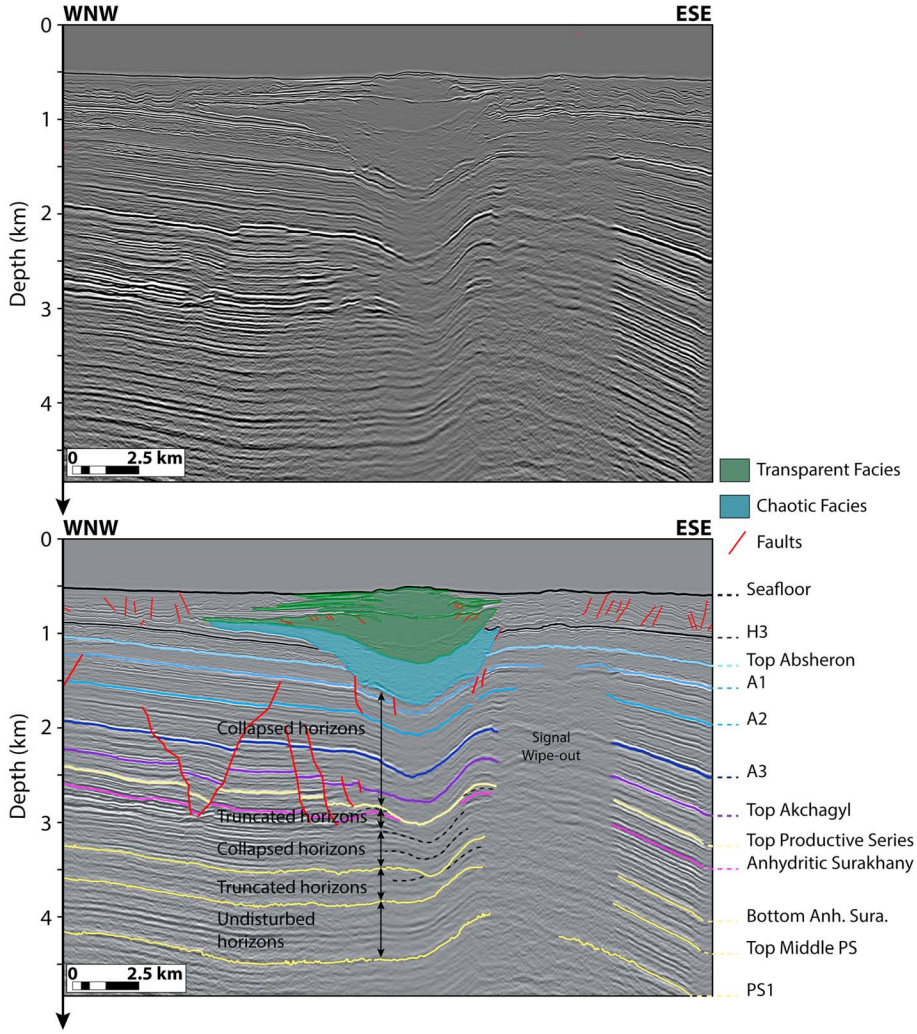

Figure 6. Uninterpreted and interpreted seismic line south of the mud volcano center. The gas blanking effect reduces below the mudflows. The transparent and chaotic signals are still present. A bending of seismic horizons from 1.5 to 3 km is noted forming a bowl-like geometry. Horizons of the upper part of the Anhydritic Surakhany are truncated by younger intervals as well as a 400-m-thick interval in the lower part of the Upper Productive Series. Horizons recover their continuity and their flat geometry below 3,800 m in the Productive Series. See Figure 3 for location.

Two main eruptive events can be distinguished (one seismic phase between the two green blocks in Figure 6). This can be due either to a quiescent phase of the MV activity when normal sedimentation was recorded or to very high sedimentation events, such as mass-flows, that can drap MVs (Deville et al., 2006). The continuity of the seismic horizon separating the two mud masses is in favor of a normal sedimentation and does not seem related to any sediment instability present during the Post-Absheron interval (Imbert et al., 2014). Normal faults flank the bowl-shaped area from 1,500 to 2,000 m and show the motion toward the center of the bowl-shaped geometry.

Thus, the main feature is the presence of a bowl-shaped geometry in the Absheron interval, truncating the upper part Anhydritic Surakhany as well as the lower part of the Upper PS where some of the horizons are discontinuous and downlap on the younger intervals. Seismic continuity then extends into the Middle PS, and some normal faults are imaged around the edges of the bowl-shaped area.

4.2. Physical, Sedimentological, and Geotechnical Properties of the Mud

DRX analysis (Figure 7a) reveals that all the samples contain 42.3 to 53.6 mass% of clays and micas, between 19.8 and 24.9 mass% of quartz, around 8 mass% of albite. Calcite is also a major mineral of the tested mud of which it represents 6.1 to 14.4 mass%. Pyrite is relatively constant for all the samples with around 1.5 mass%.

The clay fraction was analyzed in detail (Figure 7b) and is composed of 38 to 49% interstratified illite/smectite, 29 to 38% Illite and/or micas, and around 15% kaolinite. The rest is composed of around 5% chlorite and less than 2% smectite.

More details are provided by the results of the two fractions of the same samples (Raw > 5 μm; Raw < 5 μm; see Table 1). Even when separating the clay-size particles from the rest, the coarser fraction is still composed of 31.8 mass% of clay minerals (Figure 7) showing the presence of clay aggregates or claystone clasts larger than 5 μm that were not separated during suspension and centrifugation processes (Figure 7). The maximum amount of calcite and the only significant gypsum content are reached on this fraction with respectively 23.6 and 5.4 mass%. Comparatively with the <5-μm fraction, it also contains a greater part of chlorite with 23% of the clay fraction. Further analysis on the chlorite fraction would be necessary to conclude on its origin and the reasons for this variability as acid treatment destroys chlorite minerals.

In the fraction of particles less than 5 μm in diameter (Figure 7b), there is only 20% illite and/or micas but also more kaolinite and chlorite (23% and 13% respectively). Illite is known to form at a higher temperature than interstratified illite/smectite (Pollastro, 1993), which means that the finer fraction is composed of a smaller portion of high-temperature clay minerals than the unseparated samples but is also composed of more kaolinite and chlorite.

Peaks of carbonates have been observed in the coarser fraction of MVF1E as well as the BC05-DRX5 and the PC12a-DRX4. Sample BC05 was recovered from the top of the mud shield, while PC12a comes from the top of the mudflow (Figure 3 and Table 1). This peak could be the result of the formation of authigenic carbonate crusts due to methane bubbling through fresh mud after an eruptive phase or at the top of the structure during a dormant phase (Kopf, 2002; Zitter, 2004).

Thus, the Absheron mud is essentially composed of clay minerals and quartz particles (Figure 7). Clay minerals are not only contained in the matrix as fractions of particles larger than 5 μm also contain more than 30% of clays.

Biostratigraphic results on pollens and ostracods show a clear difference between samples collected on the MV or on mudflows and background samples (Figure 3 for location). Samples from the MV shield and the mudflow contain pollens from Miocene to Recent and ostracods from Late Miocene (PS). Conversely, background sediments when not barren contain pollens from the Pleistocene and Holocene ostracods (Post-Absheron). Diatoms were only found in shallow background sediments and mudflows, with Pleistocene to Holocene taxa. The presence of diatoms identical to those of the background in mudflows and their absence from shield samples may indicate that the flows remobilized surface sediments on their way downslope and mixed with them. Nannofossil results are not considered reliable due to the poorness of elements present in the samples. Put together, these biostratigraphic results seem to indicate that the mud expelled at the AMV only comes from the PS.

Samples for oedometer tests were initially selected based on MVF1 CPT data from the Absheron mudflow (Figure 3 for location, Total proprietary report, G. Dan & S. Po, 12/09/2017, personal communication). CPT curves (cone resistance, pore pressure, and friction) present four intervals with distinct evolution of the three measured parameters. We suppose that these distinct tendencies are related to different intrinsic mechanical behavior of the mud intervals and oedometer tests were run on one selected reconstituted sample per interval at water content of around 1.5 wL in order to test this hypothesis (Tables 1 and 2). Details on preparation and results of these oedometer tests are presented in Table 2. Oedometer tests presented in Figure 8a show no distinct behavior except for the MECA 10 sample, which also has a slightly different granulometric curve than the other three selected samples (Figure 8c). Indeed, the MECA 10 sample has a greater fraction of fine material (from 2 to 10 μm) and less coarse fraction (from 30 to 300 μm) than the three other samples. This also matches with the high initial void ratio and the high compressibility of the MECA 10 sample with respect to the other samples (Figure 8a). Likewise, natural sediments show similar hydraulic conductivity with void ratio results except for MECA-10 that has a slightly lower permeability trend in accordance with the lower granulometry of this sample (Figures 8b and 8c).

MECA 6-15-22 compressibility curve (equation (8)) was considered as representative of all the other natural mud samples given the very low variability between the three different samples (Figure 8a) taken from different depths of the MVF1 core (Table 1).

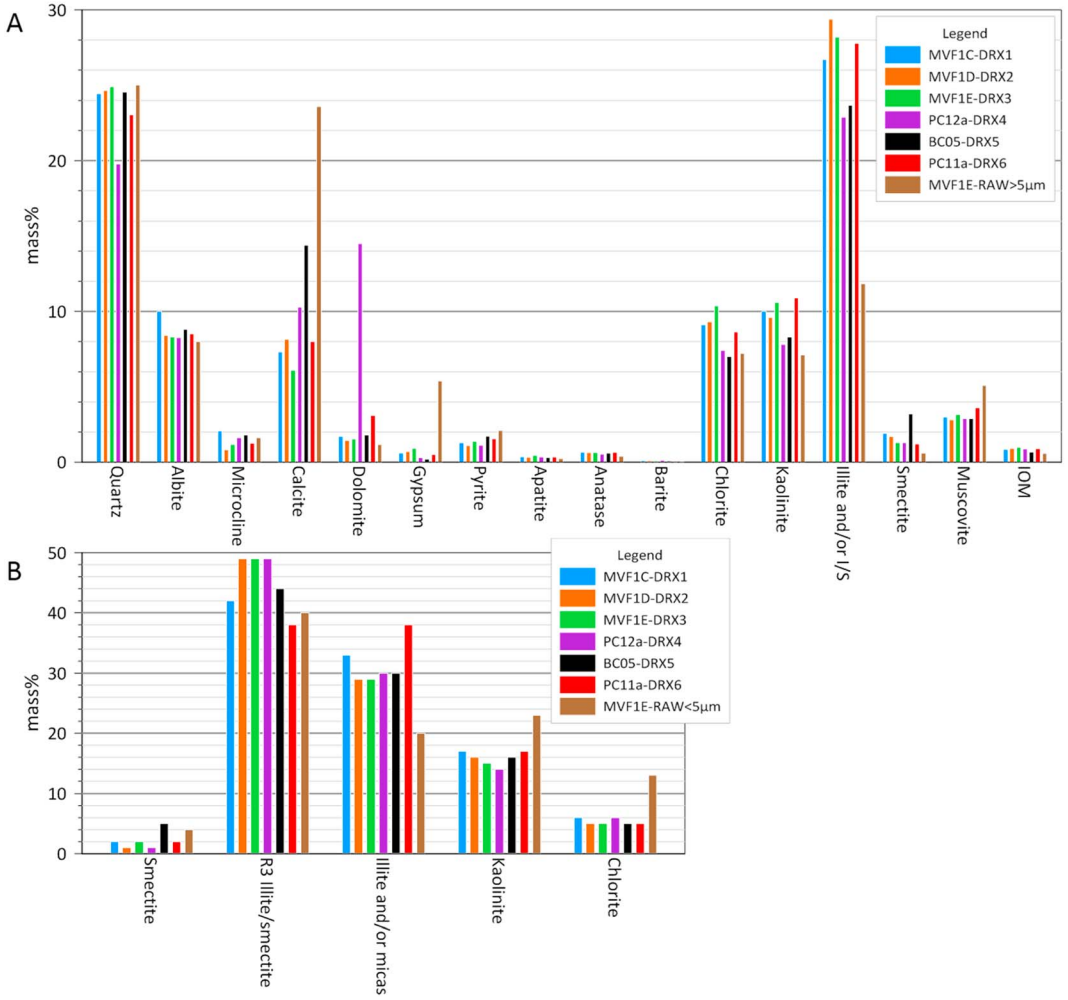

Figure 7. (a) Whole rock mineralogical analysis for all the samples collected except the less than 5-µm fraction of the MVF1E-RAW sample. The main elements composing the mud are clearly clay minerals and quartz particles. (b) Mineralogical composition of clay for all the samples collected except the MVF1E-RAW>5 µm. Globally, clay fraction is mainly composed by up to 50% of interstratified illite/smectite, 30% of Illite and/or micas, 15% of kaolinite, and a minor part of chlorite and smectite. The less than 5-µm fraction of the MVF1E-RAW sample differs from the whole samples as they have less illite and/or micas, and more kaolinite and chlorite. See Figure 3 for location map and Table 1 for details of samples.

$$e = 1.64 - 0.16 \ln\left(\frac{\sigma'_v}{\sigma'_{v0}}\right) \tag{8}$$

Permeability results showed no real differences between the different natural samples except for MECA-10 (Figure 8b), and a global linear regression for the other natural samples between ln(K) and the void ratio was adopted:

$$\ln(K) = 3.06e - 22.48 \tag{9}$$

Figure 8a shows that oedometer tests carried out on natural mud with a coarser fraction are characterized by a relatively low compressibility with a low initial void ratio (Table 2). At around 1,000 kPa of vertical effective stress, the different compressibility curves converge at the same void ratio (Figure 8a). The permeability globally increases with the fraction of coarser material with the same parallel trend as natural sediments (Figure 8b).

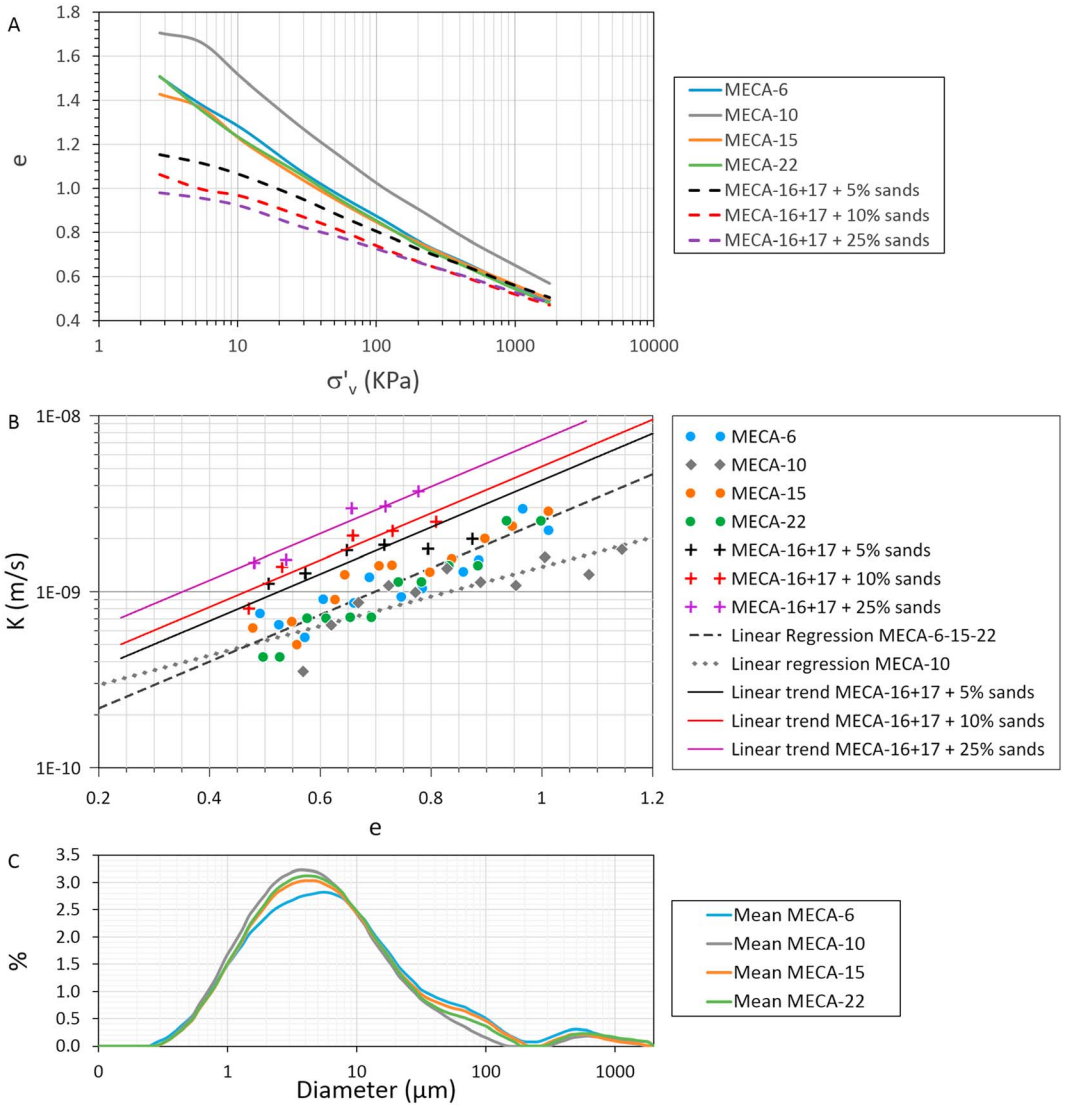

Figure 8. (a) Oedometer tests with void ratio (e) versus vertical effective stress (σ'_v) for the different tested samples. For the natural samples, only the MECA-10 has a higher compressibility and a higher initial void ratio than the other samples. The input of coarser materials reduce the initial void ratio and reduce the compressibility of the samples. (b) Hydraulic conductivity (k) versus void ratio (e) resulting from oedometer test and falling head method results for the different samples analyzed. Again, MECA-10 has a lower permeability than other natural samples, which fit the same trend. The input of coarser material increases the hydraulic conductivity but the general trend stays parallel to natural samples. (c) Cumulative granulometry for the natural samples showing that MECA 10 is finer than the three other samples. See Figure 3 and Table 1 for more details on the samples.

4.3. In Situ Lithology, Temperature, and Excess Pore Pressure Derived From In Situ Well Data

The Post-Absheron interval and the Upper part of the Absheron Suite are composed of claystone. Interstratified claystones and siltstones form the rest of the Absheron Suite and the Akchagyl Suite. The ASF extends from 2,501 to 2,887 m TVD/MSL in well B and 2,522 to 2,905 m TVD/MSL in well A. It is composed of claystone and evaporitic beds (mainly anhydrite and halite) and a minor part of siltstone. Over the 400 m of drilled Anhydritic Surakhany, 30% of evaporitic beds were encountered with individual thicknesses ranging from less than 1 to 8 m. Finally, the rest of the PS varies from claystone with rare pluri-decimetric to metric beds of siltstone to sandstone in the Surakhany (Upper PS) to interstratified claystones, siltstones, and sandstones in the Lower PS. Some of the sandstone beds reach 15 m in thickness.

Table 3 shows the results of NTG calculations based on well B data. The maximum NTG is reached for the Balakhany-Fasila interval (layer 2 in the numerical model), with a 24% NTG. The Surakhany interval has only 8% of NTG, and the Novocaspian-Absheron interval has the smallest NTG with 5%. As the well ends in the NKG interval, the NTG calculation for this particular layer may be inaccurate. From equations (3) and (5), vertical and horizontal hydraulic conductivities were calculated based on sonic logging. The calculated values fall within the measured ranges of oedometer tests on samples having a coarse content selected on the base of the NTG value of each interval.

Moreover, an unstable interval was crossed during the drilling of the ASF in well B. This interval is described as a swelling claystone and is interstratified between two 5-m-thick evaporite layers. A high acoustic velocity and abnormally low electric resistivity characterize it. Cuttings from the interval present a rather similar mineralogical composition to the mud analyzed in this study (Figure 7) with 18.5 mass% of quartz, 34 mass% of clays and micas in which there is 35% illite and/or micas, and 25% kaolinite and no smectite. However, some fractions vary from the mud analyzed: 12.8% of anhydrite were measured in the unstable interval; none was detected in the mud. Similarly, chlorite is present at 30% of the total clay fraction when in the mud, less than 10% was measured as well as calcite, which was present at 20 mass% at the considered interval, when around 10 mass% was measured in the mud.

During drilling, temperatures were also measured at different points of the well allowing to approach a geothermal gradient of 16 °C/km.

Both wells, which are located 9.5 km west of the MV (Figure 9), are overpressured at only 200 to 300 m BSF and remain in an overpressured state down to the well bottom. Overall, shale overpressure increases more or less linearly down to the top PS with a gradient of 3 MPa/km. Deeper down, the increase is linear again, with a higher gradient. In addition, six pressure peaks, that are located all along the PS Interval, can be observed in both wells (Figure 9). On these intervals, shale pressure values nearly reach the fracturing pressure, making the concerned intervals easier to fracture if pressure buildup happens. The concerned formations are the Anhydritic Surakhany (peak 1 in Figure 9) as well as five other intervals of the PS.

We noted potential links between structural features and pressure peaks (Figure 9). For instance, the pressure peak 4 in well A is split into two minor peaks in well B. There is a normal fault cut by well B that matches the pore pressure decrease observed at well B. Moreover, pressure peaks can be transposed below the MV to visualize which intervals are more prone to overpressure below the structure.

Pressures were also recorded in the reservoirs. In well A, reservoirs tested above 5,000 m BSF are in equilibrium with surrounding shales. Below 5,000 meters, in wells A and B, reservoirs are at least 20 MPa below the surrounding shales. In well A, some of these deep reservoirs are as overpressured as the shales. These results show that shallower reservoirs are not able to dissipate overpressure, whereas deeper ones appear drained and their pressure is much lower than surrounding shales. The deeper reservoir intervals are known to be regionally continuous and some even outcrop onshore in Azerbaijan (Javanshir et al., 2015). They act as regional drains for overpressured fluids with a northward hydraulic gradient (Bredehoeft et al., 1988; Javanshir et al., 2015). The sands in the northern area of the SCB are at hydrostatic pressure, while an excess hydraulic head creates deeper in the center of the basin.

4.4. Numerical Calculations of Transient Pore Pressure and Methane Diffusion

4.4.1. 1-D Modeling

The first step of the numerical modeling was a one-dimension calculation of sedimentation-generated overpressure in the deep part of the basin, 25 km south of Absheron. For this purpose, each layer was characterized by a compaction-corrected sedimentation rate based on Green et al. (2009) sediment ages and present thicknesses, compressibility, and permeability laws (Figure 10). Nadirov et al. (1997) gave average sedimentation rates for the SCB also based on present seismic thicknesses. Their estimated rate values span from 1 to 3 km/Myr for the Quaternary and around 0.5 km/Myr for the PS interval. These values are too low considering the results of our compaction-corrected 1-D modeling (Figure 10). However, our sedimentation rates depend on the compressibility laws integrated in the model. In the present paper, we present compressibility behavior of samples artificially created from natural mud and a known fraction of sand. Compressibility laws for natural sediments of each modeled stratigraphic interval might be different from the laws used in this study.

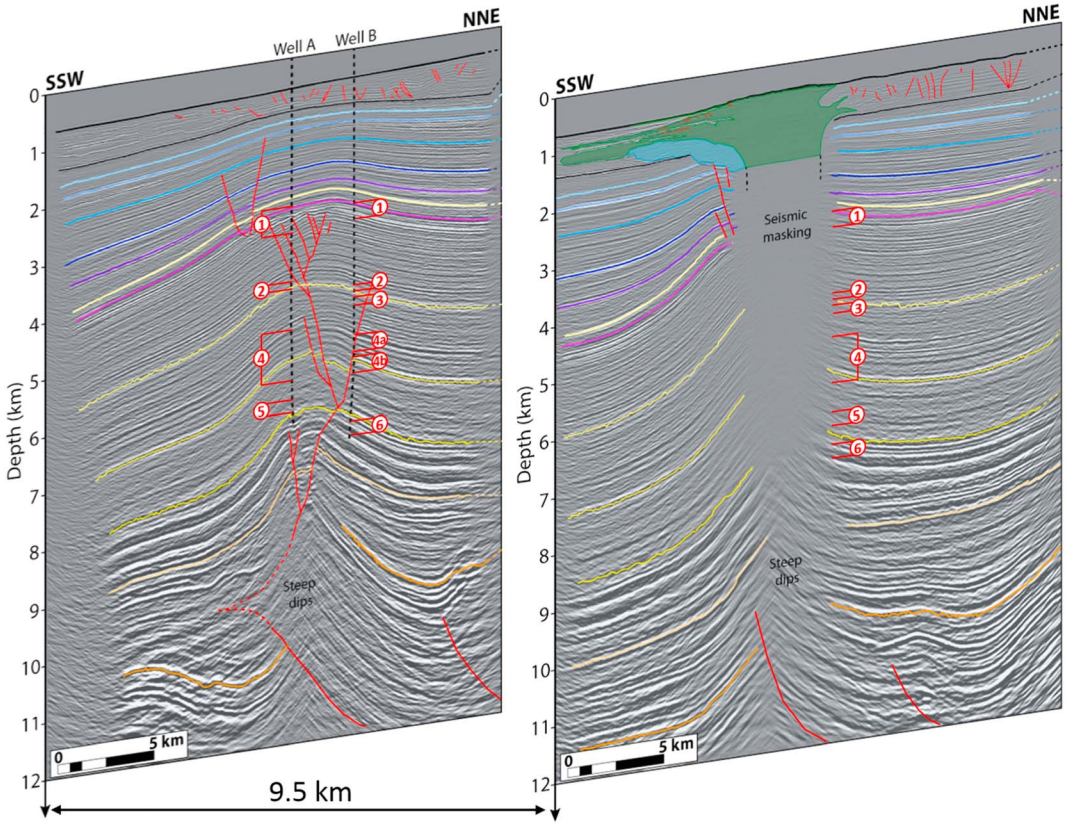

Figure 9. 3-D view of the two parallel seismic lines distant of 9.5 km. The right one is described in Figure 5. The left one in Figure 4. The pressure peaks numbered from 1 to 6 and observed on the pressure logs recorded on the two exploration wells are reported in front of the corresponding interval on seismic.

The calculation runs over 5 Myr, during which 9,600 m of compacted sediments have been deposited. As compression laws for mixed mud and very fine sands were measured for the first 1,800 kPa of vertical effective stress, at higher effective stress, the void ratio may reach negative values in some layers. In order to avoid this type of problem, we set a minimum limit for the void ratio at 0.1 in the software to obtain a compressibility trend similar to the ones presented by Chong and Santamarina (2016). Permeability laws for natural mud and mud mixed with very fine sands obtained from oedometer test results were integrated to characterize each stratigraphic interval (Figures 8a and 8b). The validity of the permeability laws was confirmed by the calculations on sonic logging (Table 3).

Figure 10 shows the porosity profile versus depth at the end of the sedimentation history. It gives a good representation of how sediments have compacted during the sedimentation history. The overpressure plot shown in Figure 10 corresponds to the overpressure generated by high sedimentation rates in the deepest part of the basin. Overpressure rises rapidly with depth in the low permeability layer 5 as overpressure cannot be evacuated and transmitted rapidly to the whole interval. The increase is slower from layer 4 down because of higher permeability. Finally, overpressure increases with a very low gradient from layer 2 below, layer 2 having the highest permeability.

4.4.2. 2-D Modeling

The second part of the modeling consisted of creating a structural model for two-dimensional diffusion of overpressure and methane. The structural model presented in Figure 11 is based on the work of Green et al. (2009) and on the fault network observed on the reference section in Figure 4. The initial section presented by Green et al. (2009) was only reproduced from the deeper part of the basin to the Absheron Ridge, where the seafloor is shallowest. The direction is the same as the section presented in Figure 1b. The total length of the section is 55 km, and its maximum depth 9.6 km. Faults shown in Figure 11 are

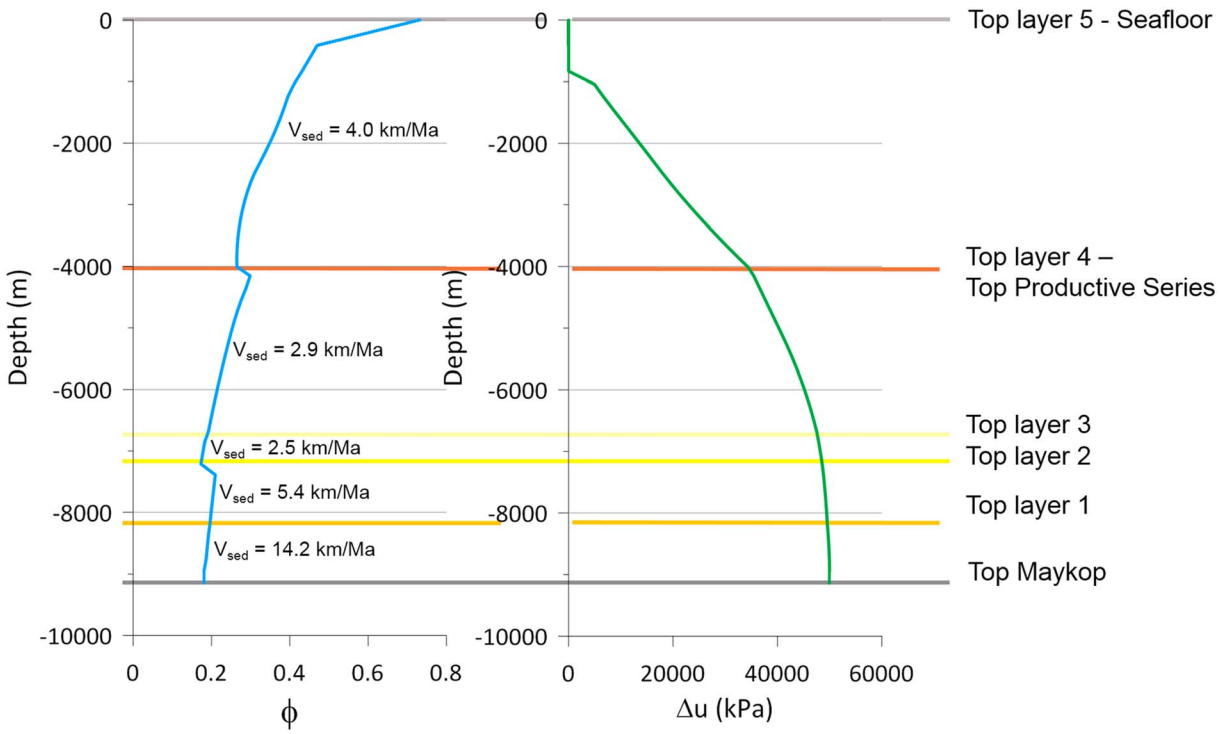

Figure 10. Results of the one-dimensional sedimentation modeling. On the left, porosity versus depth trend at the end of the 5 Myr of sedimentation with corrected sedimentation rates for each layer. On the right, overpressure versus depth trend at the end of the 5 Myr of sedimentation.

meant to represent not only the fault surfaces (localized thin shear zone) but also to the damage zone surrounding them. We estimated the thickness of the damage zone based on the work of Savage and Brodsky (2011), who relate the damaged thickness around a fault to the throw of the fault. With a total throw about 2 kilometers for the main thrust, a damage zone of a few hundred meters is expected. In the present work, a damage zone of 300 m is considered as representative of the fault zones.

Figure 11 shows the boundary conditions used for the numerical calculation of methane and pore pressure diffusions. No lateral or vertical exchange of pore pressure and methane with the outside of the model is permitted through the laterally impermeable southern and northern borders and the vertically impermeable upper and lower borders. The seawater has a fixed pore pressure of 0 kPa and a methane concentration of 10^{-5} mM (millimolar, 1 molar corresponding to a solution of 1 mol/L of concentration), which is a mean oceanic value (Lamontagne et al., 1973). The pore pressure calculated in one dimension from sedimentation with SeCoV3 (Figure 10) is imposed at the southern border of the model, where the sedimentary column is the thickest. Finally, a methane concentration of 10^{-3} mM is fixed at the bottom of the fault network, methane being generated in the Maykop Formation, the regional source rock, the deepest layer represented in the model.

Pressure and methane migration calculation were run over 5 Myr. Results of the diffusion equation resolution (equations (6) and (7)), in terms of overpressure migration, are shown in Figure 12a. Methane concentration and ratio between overpressure and vertical effective stress are shown together in Figure 12b in order to compare possible hydrofractured zones with high dissolved methane saturated areas.

Overpressure (Δu) propagated from south to north of the model at different diffusion rates. Indeed, depending mainly on permeability laws, overpressure will propagate more or less quickly and in different directions. For instance, in layer 5 overpressure did not accumulate (Figure 12a). This layer being the youngest, it maintained a high void ratio and so a higher permeability. The effect is amplified by the ratio between horizontal and vertical permeabilities. Layer 5 having a ratio of 2,200 (Table 3), the horizontal permeability in the model is 2,200 times larger than the permeability defined by oedometer test results. Therefore, in layer 5, pressure diffusion is mainly horizontal and the seawater condition (no overpressure) has significant impact on the overpressure values of this interval. From layer 4

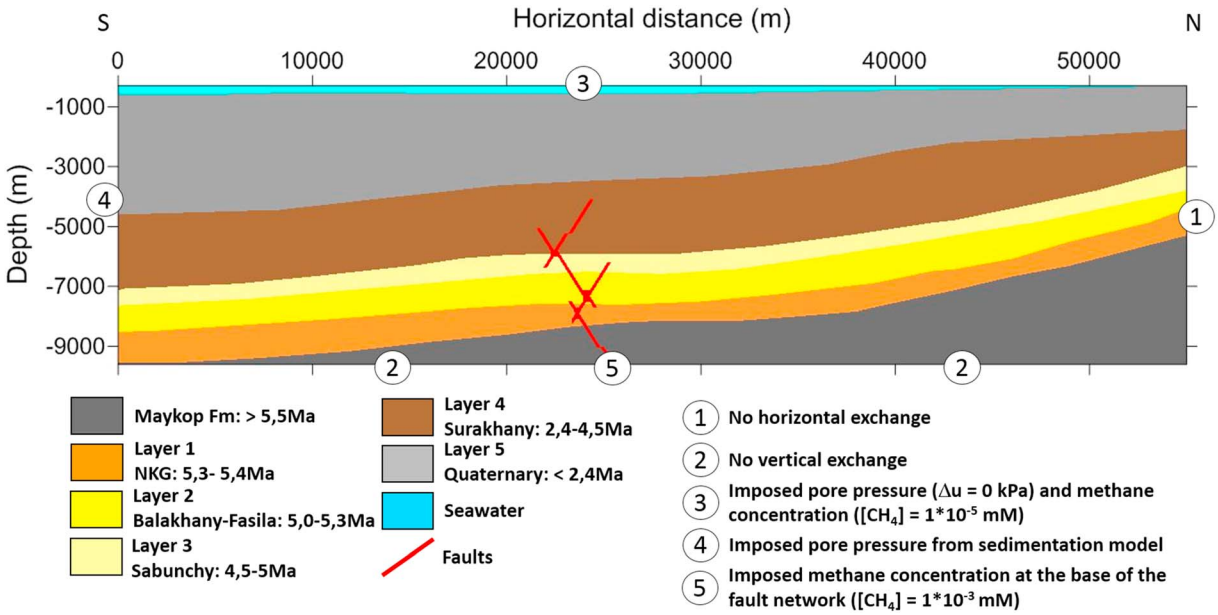

Figure 11. Structural model based on Green et al. (2009) work and on the fault network observed in Figure 4. The line follows the same trend as the seismic section of Figure 1b. Eight layers extend along the section corresponding to different sedimentation rates, compaction laws, and permeability trends (see Figure 10). The layers NKG, Balakhany-Fasila, Sabunchy, Surakhany, and quaternary are named layers 1 to 5, respectively, in other figures. Numbers showed at the limits of the model correspond to limit conditions imposed for the diffusion of pore pressure and methane.

below, the pressure is mainly diffused laterally creating a pressure front. At a given distance from the south of the model, where overpressure was injected from one-dimension sedimentation modeling (Figure 11), overpressure is larger in layer 4 than in other layers reproducing the pressure peaks observed at the wells (Figure 9).

Faults and associated damage zones were designed to rapidly diffuse methane therefore artificially reproducing methane advection through fractured zones. Methane was injected at the base of the fault network with a concentration of 10^{-3} mM (Figure 11). Methane molecular diffusivity in the rest of the model is 3 orders of magnitude lower than in faults. As a result, methane rapidly saturated the area adjoining the faults, and then diffused slowly through the sedimentary column until saturating an area nearly 2 km wide around the fault network (Figure 12b). The ratio of overpressure over vertical effective stress ($\Delta u / \sigma'_v$) is higher in layer 5, particularly in the north of the model. As it is the shallowest interval, σ'_v is the lowest of the model. Besides, little overpressure accumulation was possible in layer 5. Nevertheless, values are high at the top of the layer 4, where the ratio varies between 0.5 and 0.6. So we expect critical values in the area of high methane saturation at the Absheron crest.

5. Discussion

5.1. What Is the Stratigraphic Source of the Mud?

The geomorphological description of the AMV evidenced a bowl-shaped geometry below the mass extruded through the Absheron interval (Figure 6). This feature is formed by the Anhydritic Surakhany horizons that terminate as truncations (Catuneanu et al., 2009) below the younger seismic horizons of the Upper PS. Truncations are also observed 500 m below, in the lower part of the Upper PS. Horizon continuity resumes in the Middle PS. This particular geometry was already described and corresponds to a depleted area forming a potential former mud generation zone (Dupuis, 2017; Kirkham et al., 2017b; Stewart & Davies, 2006). The presence of two truncated intervals (Figure 6) indicates that there may have been several mud generation stages.

The unstable interval drilled in the Anhydritic Surakhany has a mineralogical composition similar to the mud analyzed in this study (Figure 7), with nearly 50% of clay minerals. Mud sampled at the seafloor is poorer in anhydrite, chlorite, and calcite than the unstable interval analyzed in the ASF. The mineralogical differences may be explained by the different paths and histories of the samples. Mud was driven upward

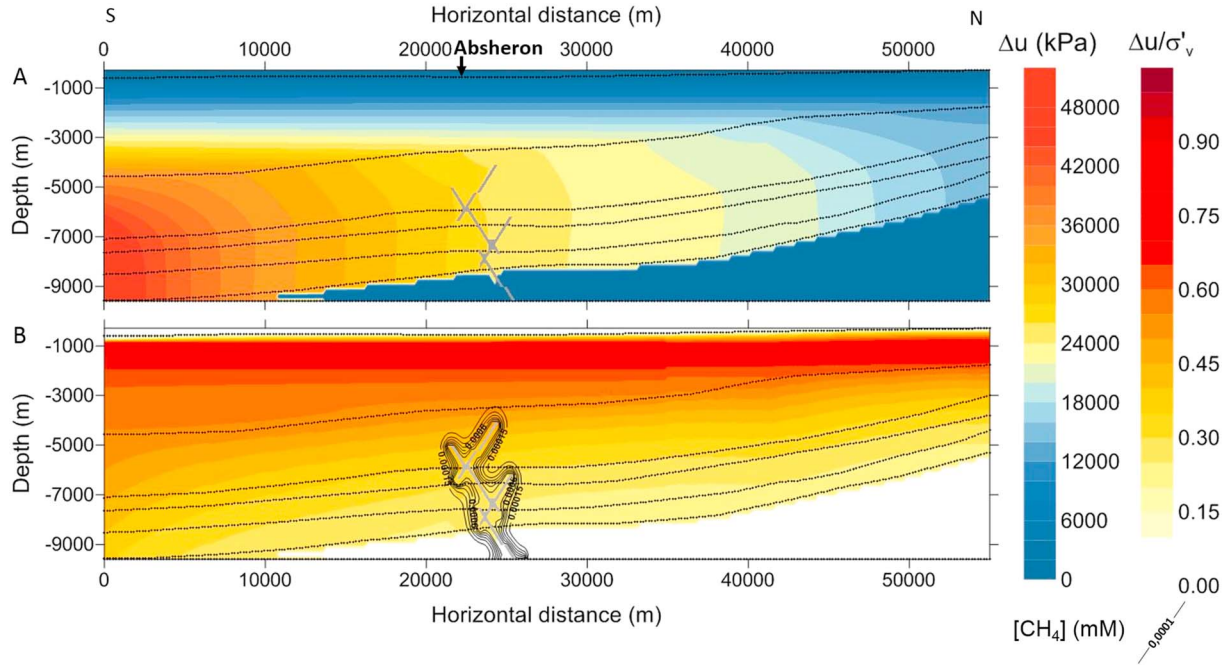

Figure 12. Results of overpressure and methane migration modeling after 5 Myr of calculation. (a) overpressure (Δu) in kPa after 5 Myr of migration through the structural model presented on Figure 11. Overpressure migrated more rapidly through layer 4, which has a higher permeability. (b) $\Delta u/\sigma'_v$ contours with values exceeding 0.75 and potentially reaching the level of hydro-fracturing. High values located in layer 5 are due to the low σ'_v near the seafloor. The black lines correspond to methane concentration contours. The top of the methane-saturated area corresponds to a zone where hydro-fracturing may occur if overpressure was slightly higher. The black dotted lines are for layer limits.

and deposited at the seafloor after a catastrophic event leading to remobilization of deep sediments. Thus, it potentially interacted with seawater but also with deeper fluids and gases forming for instance carbonate crusts at some methane seeping points or during diffuse degassing after a mud eruption (Kopf, 2002; Zitter, 2004). Conversely, the unstable interval cuttings were extracted directly from the formation through the drilling process and were in contact with the drilling mud.

From the biostratigraphic analysis of the mud and recent background sediments deposited at the seafloor, we can infer a Late Miocene to Pliocene (PS) origin for the mud.

Mineralogical analysis showed that fine fraction is poorer in illite and micas than unseparated samples (Figure 7b). These minerals are high-temperature minerals compared to smectite or interstratified illite/smectite (Pollastro, 1993). Unseparated samples are composed of a non-negligible fraction of diverse clasts when the fine fraction extraction is constituted of mud matrix particles. Therefore, clasts and coarse particles may find their source deeper than the mud matrix. However, the presence of a larger percentage of chlorite in the fine fraction (Figure 7b) tends to show a degradation of micas and illite in the mud matrix. The contact of deep fluids and seawater with the mud matrix particles may be responsible for this reaction, while coarser particles and clasts may preserve better illite and micas. Thus, mineral reactions with deep fluids and seawater could explain the different mineralogical compositions between mud matrix and clasts and they might come from the same depth magnitudes.

The Anhydritic Surakhany interval has several particularities. First, it is composed of 30% of evaporitic beds that can reach up to 8 m in thickness. The rest is mainly composed of claystones. An unstable interval was noticed during drilling, but others may exist in the Anhydritic Surakhany. Therefore, this interval may have a specific mechanical behavior. Moreover, the thermal gradient approximated from the temperatures measured at the wells is 16 °C/km, which is in accordance with mean thermal gradients measured at other SCB locations (Ginsburg et al., 1992). Considering that the MV activated after deposition of H3 (Figure 6), and considering that the thermal gradient remained constant during the Quaternary, the Anhydritic Surakhany temperature was around 30 °C when the first eruption occurred. Day-Stirrat et al. (2010) state that above 80 °C, chemical compaction (cementation processes and precipitations) will strengthen the

mudstone fabric and this process is irreversible, so the mudstone can no longer behave in a ductile way. Thus, the ASF would have been well within the temperature range where ductile deformation is conceivable.

Finally, overpressure logs show that the Anhydritic Surakhany forms a pressure peak at both wells (Figure 9). Rupture in this interval would happen earlier than in other formations for a given pressure increase or stress decrease. The fact that highly overpressured mudstones are blocked between meter-thick layers of evaporites may explain the weak behavior of some layers. As compaction water cannot be expelled vertically because of evaporites, these layers are likely to stay undercompacted and overpressured.

From these observations and measurements it seems plausible to conclude that Upper PS, and more precisely the ASF, is the source of the solid fraction of the mud expelled at the AMV.

5.2. How Do the Field Pore Pressure Measurements Compare to the Model?

It is quite clear on pressure logs that pressure regimes are completely different in shales and in reservoirs. Indeed, shales are highly overpressured all along the well, following a trend nearly parallel to the lithostatic pressure from the Top Akchagyl to the Bottom PS. In the bottom part of the wells (from the PS2 seismic horizon downward), overpressure level in shales remains rather constant, while reservoir pressures are nearly hydrostatic. Javanshir et al. (2015) describe similar pressure regime and magnitudes in the neighboring Shah Deniz fold. The Upper PS there have equal sandstone and shale overpressures and as the reservoir facies become more abundant and continuous in the Bottom PS, they become less overpressured. Therefore, in Shah Deniz and Absheron, the deep reservoirs seem to act as permeable drains as they allow overpressure to dissipate. The fact that shale pressure is also affected shows that dewatering might occur in the thinner shale intervals contained in the Bottom PS. Indeed, the abundance of permeable reservoirs would allow compaction water to be drained away from the shales, reducing their pressure. There is lateral pressure transmission from the deep part of the basin to the edges through regional-scale reservoirs (Javanshir et al., 2015), from the south to the north of the sections presented in Figure 9.

However, pressure horns in Absheron shales are not recorded in the data of Javanshir et al. (2015). Some intervals of the PS of Absheron wells are more overpressured than the rest of the stratigraphic interval. These peaks bring the corresponding intervals to pressure values between 5 and 10 MPa below hydrofracturing pressure in wells located 9.5 km from the MV center. The difference between hydrofracturing pressure and shale pressure may be even smaller near the MV, or it may have been smaller in the past, before MV activation. Therefore, they represent weak areas where a local rise in overpressure through clay dehydration or tectonic overpressuring for instance (Osborne & Swarbrick, 1997), or a drop in effective stress (erosion or fold growth and crestal uplift) could generate hydrofractures.

Pressures recorded in the two wells are not exactly the same: in the southern well (Well A), shale pressure decreases more gently within the Bottom PS and reservoir pressures are higher. Moreover, pressure horns are stronger in well B (to the north). Differential sedimentation between the deep basin located at the south of the Absheron anticline and the northern edge of the basin where less sediments accumulate could explain this phenomenon (Grosjean et al., 2009; Javanshir et al., 2015). As pressure transmission is oriented roughly from the south to the north of the anticline, the northern side of the anticline would accumulate more overpressure in the shales, whereas reservoirs would be more drained than in the southern flank. This phenomenon was also noted at the neighboring Shah Deniz anticline (Javanshir et al., 2015).

Two-dimensional model sections reproducing the main features of the pressure plots are shown on Figure 12. The overpressure rises down to 2,000 and 5,000-m deep depending on the location. Then overpressure remains constant at 30 MPa at the Absheron location and even decreases to 25 MPa when reaching the bottom part of the PS where highly continuous and abundant reservoir facies are present. Moreover, the numerical modeling results emulate the Top Surakhany pressure horn. Yet the modeling results underestimate the overpressure at the Absheron location (Figure 12a) as they are not in accordance with overpressure values recorded at the wells. Indeed, from Top Surakhany down, overpressure reaches values between 20 and 50 MPa. The discrepancy between measured and calculated overpressures may be related to the compressibility and permeability laws applied to the model, which were obtained from artificial

(reconstituted) sandy-clayey samples and not from natural samples from the different stratigraphic layers. Besides, the considered source of overpressure is related to fast sedimentation and might not be sufficient to model the natural pressure conditions of the Absheron anticline. Indeed, additional sources of pore pressure may play an important role and are yet to be considered in the modeling work.

However, and as a first approach, the present calculation was able to reproduce the main overpressure trends visible at the wells.

5.3. How Does Methane Diffusion Interact With Excess Pore Pressure Accumulation?

Modeling results shows that high values of $\Delta u / \sigma'_v$ fit with high dissolved methane concentrations and occur around the fault network below the AMV (Figure 12b). The consequence of high $\Delta u / \sigma'_v$ causing hydrofracturing may be an important decrease in pore pressure leading to methane exsolution and expansion (Duan & Mao, 2006) and generation of overpressured mud. Gas exsolution in sediments has proved to be a critical factor controlling sediment damage. Indeed, experience on gassy sediment core recovery in deep water shows important damage and loss of structure during the core ascent to the surface and associated hydrostatic pore reduction (Sultan et al., 2012). Loss of acoustic signal corresponding to the presence of free gas correlates with dramatic decrease of the yield stress ratio illustrating the damage made to the sediments.

Moreover, the presence of normal faults at the anticline crest between the Upper PS and the Top Absheron (Figure 4) shows that the state of stress where the primary source of mud was identified was extensive at the time when the AMV formed. If compressive state was dominating at these time and location, the observed faults must have been thrusts. Therefore, σ_1 (the maximum principal stress) was certainly vertical, so the least principal stress was horizontal. Fractures open in the direction of the least principal stress and then propagate in a plane perpendicular to this direction (Hubbert & Willis, 1957). Thus, hydrofractures generated at the time of the MV formation above the mud generation zone are expected to be vertical.

A present-day studied example of clastic extrusion triggering displays similar results. Indeed, the Lusi disaster, whose 2006 triggering cause is still a matter of debate between an earthquake and drilling issues (A. Mazzini et al., 2007; M. Tingay et al., 2008, 2017), was initiated by the combination of under-compaction/overpressure in the source layer and the presence of dissolved and free gas. According to Davies et al. (2008), fractures generated by drilling activities have caused an important decrease in pore pressure and the consequence was gas exsolution and expansion, overpressured mud generation, and the extrusion of mud to the surface (Davies et al., 2008). However, Mazzini et al. (2012) proposed a hydrothermal source for the gas, and yet Lusi triggering is already explained by gas flowing in undercompacted and overpressured sediments.

Thus, we suggest that the theoretical mechanism we propose for mud generation and extrusion with a combination of potential fracture zones and gas-saturated areas would also be applicable to the Absheron fold, where the studied MV is located.

5.4. What Is the most Plausible Sequence for the Formation of the AMV?

Based on previous observations and conclusions, a qualitative formation model for the AMV is proposed. This model is developed in five main phases:

Phase 1: rapid deposition of the PS (over 3.5 km in 2 Myr) above the gas-mature Maykop Formation that would generate hydrocarbons migrating slowly through the sedimentary column (Figure 13-1). Maykop Formation started generating gas during the Late Miocene in the Shah Deniz region located less than 50 km from Absheron gas discovery (Figure 2.9 in Alizadeh et al., 2017). Moreover, the deposition of the ASF proves that the sea level must have been lower than nowadays at the end of the PS deposition.

Phase 2: folding started during deposition of the Akchagyl Suite. It is linked to the propagation of a deep thrust terminating in the Maykop formation and linked to normal faults related to the fold formation. Methane migration is then focused into the faulted core of the anticline (Figure 13-2). The folding also has the effect of generating preferential rupture zones at its crest (Figure 13-2). Indeed, at the anticline crest, σ'_v is lower than on the flanks. Besides, as more space is available for sediment deposition in the surrounding synclines and in the deeper part of the basin, overpressure is generated and transmitted toward the

Absheron location. Overpressure generation and transmission as well as lower σ'_v at the flanks increases the $\Delta u / \sigma'_v$ ratio thereby increasing pore gas solubility.

Phase 3: $\Delta u / \sigma'_v$ ratio reaches the hydro-fracturing threshold (Figure 13-3), leading to a significant decrease in pore pressure.

Phase 4: hydrofracturing triggers gas exsolution and expansion in gas-saturated and mechanically weak layers such as ASF (Figure 13-4). Exsolution remobilizes the weak interval, generating mud. Overpressured and low-density mud is then transported to the seafloor provoking the first mud extrusion. As gas, mixed with sediments and water, migrates up the hydrofracture network, methane expands amplifying the process and potentially eroding fracture walls (Figure 13-4).

Phase 5: the process goes on with gas exsolution propagating in the Anhydritic Surakhany, depleting this layer continuously. Collapse of the upper strata into the depleted area creates the rather flat and low topography volcano (Figure 13-5). The extruded mud slowly degasses at the seafloor.

Phase 6: quiescent and active phases of the MV alternates, creating a complex interdigitation geometry where normal sedimentation predominates during quiescent phases of the volcano. Further depletion happens in the source, triggering more collapse, while more mud is extruded at the seafloor (Figure 13-6).

The initial trigger of this MV is not related to gas, as hydrofracturing due to overpressure buildup and weakness of the fold-crest initiates the succession of events. However, in this conceptual model, methane would have three essential effects.

Gas needs to saturate the porous network in its dissolved state before hydrofracturing in order to provoke remobilization of sediments. Exsolution of methane weakens and disaggregates host sediments (Sultan et al., 2012; M. R. P. Tingay et al., 2015).

As free gas has very low density (typically about 1/1,000 of that of water in normal conditions), it will flow toward the surface (Brown, 1990), carrying the mud away (solid particles and formation water).

Finally, as gas goes up into the pipe, it expands (Brown, 1990), accelerating the mud ascent, sustaining mud pressure, and eroding fracture walls, creating clasts, to end-up with mud breccia extrusion at the surface.

Thus, methane exsolution is the key to mud formation but also the main driver for mud remobilization toward the surface due to its low density and expansion capacity. Initial rupture is essential in order to start the chain reaction and methane expansion and exsolution will maintain the pipes open and even enlarge them.

5.5. Limits and Perspectives of the Study

This conceptual formation model of MVs closely fits with observations and analysis of the available data set and is partly based on the numerical modeling results presented earlier.

However, Improvements May Be Made at Several Levels:

Data Set: For instance, the seismic masking prevents direct observation of the center of the volcano's plumbing system. Reprocessing of the data was attempted several times and with different methods and approaches, but it remains challenging due to the presence of gas-charged mud and free gas. The available biostratigraphic analyses are not quantitative and for further precision on the mud origin quantitative analyses of the fauna and flora in mud will be necessary. Analysis of the clasts will also help to refine the mud origin.

Numerical modeling: The compressibility laws used in the current model could be improved to consider soil compressibility for the highest stress range (Chong & Santamarina, 2016). In the present work and in order to avoid negative void ratio values, the software limits the minimum void ratio to 0.1. In the present model, pore pressures generated by sedimentation and pressure transmission are not calculated simultaneously. Overpressure due to sedimentation is calculated over 5 Myr of sedimentation history and is integrated as a boundary condition into the 2-D Darcy's and Fick's diffusion equations. The next step would be to integrate both sedimentation and diffusion processes into one unique 2-D model. Finally, the model does not simulate the post-hydrofracturing processes causing gas exsolution and overpressured mud expulsion. Gas exsolution and expansion processes will have to be integrated into this model in order to reproduce MV initiation.

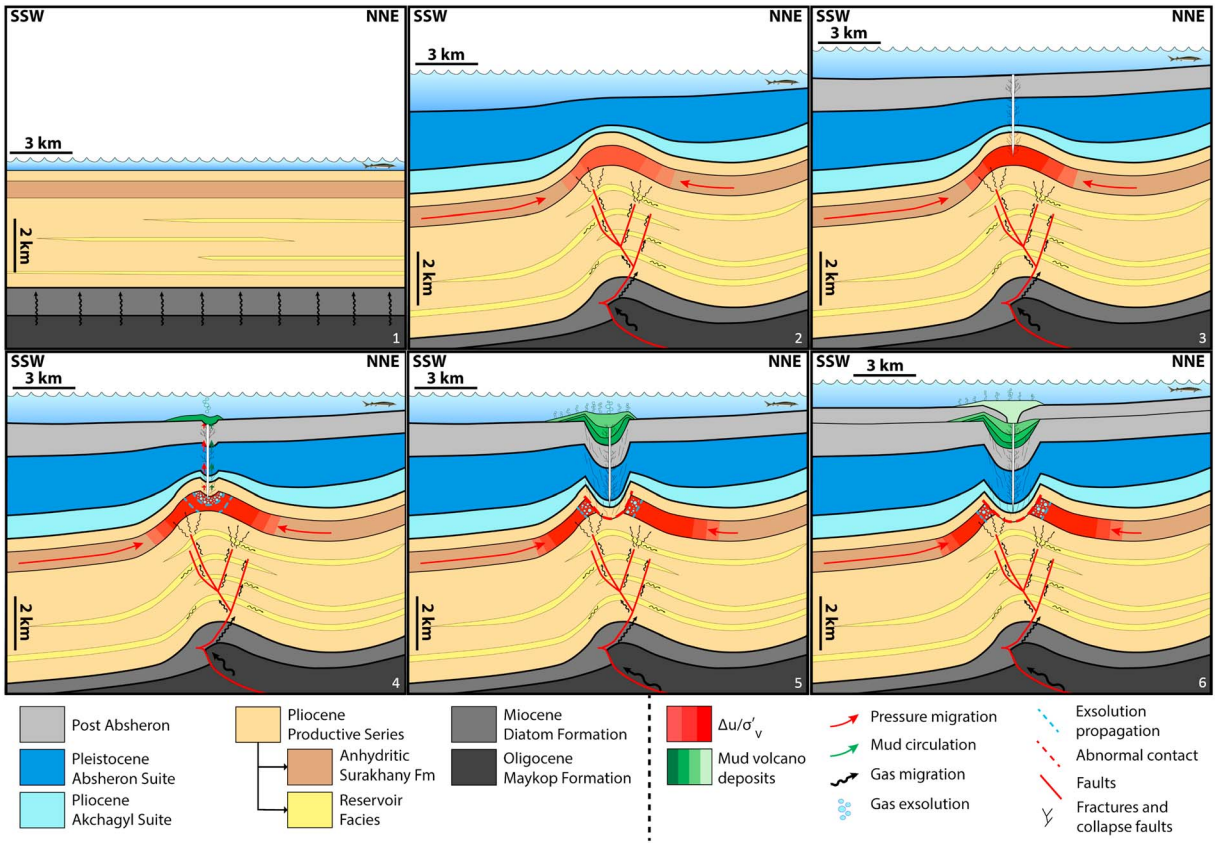

Figure 13. Formation model for the Absheron mud volcano based on in situ observations and measurements, laboratory tests, and analysis and numerical modeling. 1: Rapid deposition of the Productive Series and maturation of the Maykop formation. Slow and extended methane migration. 2: Absheron fold creation. Focusing of the methane migration through fold-related fault network and $\Delta u/\sigma'_v$ increase at the anticline crest. 3: Rupture condition reached and hydrofracturing of the sedimentary column from the seafloor to the Anhydritic Surakhany. 4: Gas exsolution and expansion and remobilization of Anhydritic Surakhany sediments. First extrusion. 5: Propagation of gas exsolution and sediment remobilization. Depletion of the Anhydritic Surakhany and collapse of the overlying strata. 6: Present geometry after alternance of several quiescent and active episodes for the mud volcano. More depletion of the source and collapse of the overlying strata is triggered at each active episodes.

Overpressure Generation Mechanisms: The MV is located at the crest of an active anticline and triggered after one of the main folding phases. Thus, lateral tectonic overpressuring is expected to have happened before the MV formation (Osborne & Swarbrick, 1997; Swarbrick et al., 2002). This tectonic overpressuring has proved to increase the global ovepressure up to 16 MPa at 3.5-km deep partly due to porosity decrease (Couzens-Schultz & Azbel, 2014; Obradors-Prats et al., 2017). Moreover, internal sources have not been considered such as clay dehydration and smectite-illite reactions that generate a large volume of water in the pore space, thus generating overpressure (Osborne & Swarbrick, 1997; Swarbrick et al., 2002). Gas generation is also considered as an overpressure generation mechanism and may have implications for this numerical model as gas is generated and diffused through the sedimentary column (Osborne & Swarbrick, 1997; Swarbrick et al., 2002). Considering these new pore pressure input, the $\Delta u / \sigma'_v$ ratio may increase drastically and the model may be able to reproduce the observed in situ pore pressure measurements.

6. Conclusions

Based on 3-D seismic data, mineralogical, geotechnical, and biostratigraphic analyses of the sampled mud together with well data, the morphological observations, we conclude that the ASF is a plausible source for the AMV. Pressures recorded at the wells show, as in Shah Deniz, that deep reservoirs act as drains for pressure provoking a decrease in overall shale pressure logs. Pressure horns were also recorded at specific intervals, as for the ASF, where shale pressure is close to the fracture limit.

Based on these observations, a numerical model with 2-D-diffusion equations was applied on a basin scale section. Sedimentation-related overpressures underestimate by 50% the pressures measured in the wells but reproduce fairly well the observed trends. Additional sources of in situ overpressure generation (i.e., clay dehydration and transformation), which are not included in the current model, may explain the discrepancy between the model prediction and the pore pressure values of wells. The main observation made through the numerical model is the superposition of methane-saturated areas with potential hydrofracturing zones. Indeed, hydrofracturing may produce a drastic decrease in pore pressure, allowing gas exsolution and expansion. Based on the present model results, on experimental results of gassy-sediment behavior in which the gas exsolution damages the sediment and reduces its mechanical strength and on the Lusi disaster studies, we conclude that the superposition of potential hydrofracturing areas and gas-saturated zones can explain that the AMV activated at the crest of the anticline.

As a result, we propose a conceptual evolutionary model for the AMV as follows: initial stages of folding focus methane migration into the anticline crest bringing methane to the upper geological layers and mainly to the Anhydritic Surakhany Fm. Pore pressure accumulation and its lateral migration through the Anhydritic Surakhany Fm. promote hydrofracturing at the location of the AMV, causing a decrease in pore pressure. Those conditions lead to methane exsolution and expansion and to upward remobilization of the already weak Anhydritic Surakhany interval, generating low density and overpressured mud. During mud ascent, gas bubbles expand, splintering fracture walls and incorporating clasts into the mud. Finally, extrusion at the seafloor happens where the mud slowly expels methane. As extrusion goes on, a collapse of the overlying strata into the depleted mud generation zone forms.

Therefore, even though the trigger point for the whole MV formation process in our model is hydrofracturing, clay-rich sediments have to be initially saturated with methane in order to generate mud. The methane is essential and has three main roles: exsolution allows creating the mud from weak layers, its low density decreases the mud one and accelerate its upward flow to the surface, and gas expansion sustains mud overpressure and causes splintering of gas-saturated fracture walls creating clasts.

With the available dense data set, we evidence that in order to form the AMV, a combination of three factors is required: high pore pressure, gas saturation and clay-rich sediments. Recent work on the Lusi eruption also demonstrated the importance of the same factors in a different geological environment. Therefore, detecting the presence of those three factors may help understand the preconditioning conditions of MV's formation.

Acknowledgments

Total S.A. is owner of the seismic and well data used and presented in this paper. Please contact the Research and Development team of Total for information and potential access to this data (SCR/RD, Total CSTJF, Avenue Larribau, 64000 Pau). Sediment analysis results used in this study can be downloaded by following this link: https://doi.org/10.6084/m9.figshare.7448153. To access the SeCoV3 software and the input parameters, please directly download it here https://github.com/ArthurBlouin/SeCoV3.git. This study was realized in the scope of the PhD of Arthur Blouin under the joint direction of the Pau University (UPPA), Ifremer and Total S.A. The authors would like to thank Claire Fialips for the mud mineralogy analysis, Jérémie Gaillot for the help with biostratigraphy interpretation, and Mickaël Rovere for the help rendered during compressibility/permeability analyses.

References

Abdullayev, E., & Leroy, S. A. G. (2016). Provenance of clay minerals in the sediments from the Pliocene Productive Series, western South Caspian Basin. *Marine and Petroleum Geology*, *73*, 517–527. https://doi.org/10.1016/j.marpetgeo.2016.03.002

Alfaro, M. C., & Wong, R. C. K. (2001). Laboratory studies on fracturing of low-permeability soils. *Canadian Geotechnical Journal*, *38*(2), 303–315. https://doi.org/10.1139/cgj-38-2-303

Alizadeh, A. A., Guliyev, I. S., Kadirov, F. A., & Eppelbaum, L. V. (2017). *Geosciences of Azerbaijan Volume II: Economic Geology and Applied Geophysics* (Vol. II). Basel, Switzerland: Springer International Publishing. https://doi.org/10.1007/978-3-319-40493-6

Allen, M. B., Jones, S., Ismail-Zadeh, A., Simmons, M., & Anderson, L. (2002). Onset of subduction as the cause of rapid Pliocene-Quaternary subsidence in the South Caspian basin. *Geology*, *30*(9), 775–778. https://doi.org/10.1130/0091-7613(2002)030<0775:OOSATC>2.0.CO;2

ASTM International. (1996). D 2435-96 - Standard test method for one-dimensional consolidation properties of soils. *American Society for Testing and Materials*, (August), 196–205. doi: https://doi.org/10.1520/D2435-96

Bahorich, M. S., & Farmer, S. L. (1995). 3-D seismic discontinuity for faults and stratigraphic features: The coherence cube. In *SEG Technical Program Expanded Abstracts 1995* (pp. 93–96). Houston, TX: Society of Exploration Geophysicists. https://doi.org/10.1190/1.1887523

Benjamin, U. K., & Huuse, M. (2017). Seafloor and buried mounds on the western slope of the Niger Delta. *Marine and Petroleum Geology*, *83*, 158–173. https://doi.org/10.1016/j.marpetgeo.2017.02.023

Bochud, M. (2011). *Tectonics of the Eastern Greater Caucasus in Azerbaijan*, (Vol. 30, p. 207). Fribourg, Switzerland: Université de Fribourg.

Boudreau, B. P. (1996). The diffusive tortuosity of fine-grained unlithified sediments. *Geochimica et Cosmochimica Acta*, *60*(16), 3139–3142. https://doi.org/10.1016/0016-7037(96)00158-5

Bredehoeft, J. D., Djevanshir, R. D., & Belitz, K. R. (1988). Lateral fluid flow in a compacting sand-shale sequence: South Caspian basin. *American Association of Petroleum Geologists Bulletin*, *72*(4), 416–424. https://doi.org/10.1306/703C9A1E-1707-11D7-8645000102C1865D

Brown, K. M. (1990). The nature and hydrogeologic significance of mud diapirs and diatremes for accretionary systems. *Journal of Geophysical Research*, *95*(B6), 8969. https://doi.org/10.1029/JB095iB06p08969

Brunet, M.-F., Korotaev, M. V., Ershov, A. V., & Nikishin, A. M. (2003). The South Caspian Basin: a review of its evolution from subsidence modelling. *Sedimentary Geology*, *156*(1-4), 119–148. https://doi.org/10.1016/S0037-0738(02)00285-3

Catuneanu, O., Abreu, V., Bhattacharya, J. P., Blum, M. D., Dalrymple, R. W., Eriksson, P. G., et al. (2009). Towards the standardization of sequence stratigraphy. *Earth-Science Reviews*, *92*(1–2), 1–33. https://doi.org/10.1016/j.earscirev.2008.10.003

Chong, S.-H., & Santamarina, J. C. (2016). Soil Compressibility Models for a Wide Stress Range. *Journal of Geotechnical and Geoenvironmental Engineering*, *142*(6), 06016003), 1–7. https://doi.org/10.1061/(ASCE)GT.1943-5606.0001482

Contet, J., & Unterseh, S. (2015). Multiscale site investigation of a giant mud-volcano offshore Azerbaijan—Impact on subsea field development. *Offshore Technology Conference*, *OTC-25864*(Mv), 1–10. doi: https://doi.org/10.4043/25864-MS

Couzens-Schultz, B. A., & Azbel, K. (2014). Predicting pore pressure in active fold-thrust systems: An empirical model for the deepwater Sabah foldbelt. *Journal of Structural Geology*, *69*(PB), 465–480. https://doi.org/10.1016/j.jsg.2014.07.013

Crank, J. (1975). The mathematics of diffusion. https://doi.org/10.1016/0306-4549(77)90072-X

Das, B. M. (2013). *Principles of geotechnical engineering*, (7th ed.. *Journal of Chemical Information and Modeling* (Vol. 53)). Boston, Massachusetts: CENGAGE Learning. https://doi.org/10.1017/CBO9781107415324.004

Davies, R. J., Brumm, M., Manga, M., Rubiandini, R., Swarbrick, R., & Tingay, M. (2008). The East Java mud volcano (2006 to present): An earthquake or drilling trigger? *Earth and Planetary Science Letters*, *272*(3–4), 627–638. https://doi.org/10.1016/j.epsl.2008.05.029

Day-Stirrat, R. J., McDonnell, A., & Wood, L. J. (2010). Diagenetic and seismic concerns associated with interpretation of deeply buried mobile shales. *Shale Tectonics: AAPG Memoir*, *93*, 5–28. https://doi.org/10.1306/13231306M93730

Deville, E. (2009). Mud volcano systems. In N. Lewis, & A. Moretti (Eds.), *Volcanoes: Formation, eruptions and modelling* (pp. 95–125 (404)). Hauppauge, New York: Nova Science Publishers.

Deville, E., Guerlais, S. H., Callec, Y., Griboulard, R., Huyghe, P., Lallemant, S., et al. (2006). Liquefied vs stratified sediment mobilization processes: Insight from the South of the Barbados accretionary prism. *Tectonophysics*, *428*(1–4), 33–47. https://doi.org/10.1016/j.tecto.2006.08.011

Duan, Z., & Mao, S. (2006). A thermodynamic model for calculating methane solubility, density and gas phase composition of methane-bearing aqueous fluids from 273 to 523 K and from 1 to 2000 bar. *Geochimica et Cosmochimica Acta*, *70*(13), 3369–3386. https://doi.org/10.1016/j.gca.2006.03.018

Dupuis, M. (2017). Processus de mise en place et évolution des systèmes de volcans de boue. Université Lille 1 - Sciences et technlogies.

Eaton, B. A. (1975). The equation for geopressure prediction from well logs. In *Fall meeting of the Society of Petroleum Engineers of AIME* (5 pp.). Dallas, Texas: Society of Petroleum Engineers. https://doi.org/10.2118/5544-MS

Egan, S. S., Mosar, J., Brunet, M.-F., & Kangarli, T. (2009). Subsidence and uplift mechanisms within the South Caspian Basin: Insights from the onshore and offshore Azerbaijan region. *Geological Society, London, Special Publications*, *312*(1), 219–240. https://doi.org/10.1144/SP312.11

Etiope, G., Feyzullayev, A., & Baciu, C. L. (2009). Terrestrial methane seeps and mud volcanoes: A global perspective of gas origin. *Marine and Petroleum Geology*, *26*(3), 333–344. https://doi.org/10.1016/j.marpetgeo.2008.03.001

Feng, T. W. (2005). *Reappraisal of the fall cone test. In Proceedings of the 16th International Conference on Soil Mechanics and Geotechnical Engineering*, (Vol. 16, pp. 357–360). Osaka, Millpress Science Publishers/IOS Press. https://doi.org/10.3233/978-1-61499-656-9-357

Fialips, C. I., Labeyrie, B., Burg, V., Mazière, V., Munerel, Y., Haurie, H., et al. (2018). Quantitative mineralogy of Vaca Muerta and alum shales from Core chips and drill cuttings by calibrated SEM-EDS mineralogical mapping. DOI: https://doi.org/10.15530/urtec-2018-2902304

Foucher, J. P., Westbrook, G., Boetius, A., Ceramicola, S., Dupré, S., Mascle, J., et al. (2009). Structure and drivers of cold seep ecosystems. *Oceanography*, *22*(1), 92–109. https://doi.org/10.5670/oceanog.2009.11

Fowler, S. R., Mildenhall, J., Zalova, S., Riley, G., Elsley, G., Desplanques, A., & Guliyev, F. (2000). Mud volcanoes and structural development on Shah Deniz. *Journal of Petroleum Science and Engineering*, *28*(4), 189–206. https://doi.org/10.1016/S0920-4105(00)00078-4

Ginsburg, G. D., Guseynov, R. A., Dadashev, A. A., Ivanova, G. A., Kazantsev, S. A., Solov'yev, V. A., et al. (1992). Gas hydrates of the southern Caspian. *International Geology Review*, *34*(8), 765–782. https://doi.org/10.1080/00206819209465635

Golonka, J. (2007). Geodynamic evolution of the South Caspian Basin. *Oil and Gas of the Greater Caspian Area*, *55*, 17–41. https://doi.org/10.1306/1205844St551463

Graue, K. (2000). Mud volcanoes in deepwater Nigeria. *Marine and Petroleum Geology*, *17*(8), 959–974. https://doi.org/10.1016/S0264-8172(00)00016-7

Green, T., Abdullayev, N., Hossack, J., Riley, G., & Roberts, A. M. (2009). Sedimentation and subsidence in the South Caspian Basin, Azerbaijan. *Geological Society, London, Special Publications*, *312*(1), 241–260. https://doi.org/10.1144/SP312.12

Grosjean, Y., Zaugg, P., Gaulier, J.-M., & Total S.A. (2009). Burial hydrodynamics and subtle hydrocarbon trap evaluation: From the Mahakam Delta to the South Caspian Sea. International Petroleum Technology Conference Held in Doha, Qatar, 7-9 December 2009, 1–12.

Guillon, S., & Keskes, N. (2004). Sismage and the 3D visualization at Total. In *AAPG International Conference* (pp. 1–3).

Guliyev, I., Aliyeva, E., Huseynov, D., Feyzullayev, A., & Mamedov, P. (2010). Hydrocarbon potential of ultra deep deposits in the South Caspian Basin. In *AAPG European Region Annual Conference* (Vol. 1, p. 66). Kiev, Ukraine.

Guliyev, I. S., Feizulayev, A. A., & Huseynov, D. A. (2001). Isotope geochemistry of oils from fields & mud volcanoes in the South Caspian Basin, Azerbaijan. *Petroleum Geoscience*, *7*(2), 201–209. https://doi.org/10.1144/petgeo.7.2.201

Hedberg, H. D. (1974). Relation of methane generation to Undercompacted shales, shale diapirs, and mud volcanoes. *AAPG Bulletin*, *58*(4), 661–673. https://doi.org/10.1306/83D91466-16C7-11D7-8645000102C1865D

Hubbert, M. K., & Willis, D. G. (1957). Mechanics of hydraulic fracturing. *Society of Petroleum Engineers*, *210*, 153–163. Retrieved from http://archives.datapages.com/data/specpubs/methodo2/data/a075/a075/0001/0200/0239.htm

Hudson, S. M., Johnson, C. L., Efendiyeva, M. A., Rowe, H. D., Feyzullayev, A. A., & Aliyev, C. S. (2008). Stratigraphy and geochemical characterization of the Oligocene-Miocene Maikop series: Implications for the paleogeography of Eastern Azerbaijan. *Tectonophysics*, *451*(1–4), 40–55. https://doi.org/10.1016/j.tecto.2007.11.045

Imbert, P., Geiss, B., & Fatjó de Martín, N. (2014). How to evacuate 10 km3 of mud: Saturate with gas and decrease the pressure! *Geo-Marine Letters*, *34*(2–3), 199–213. https://doi.org/10.1007/s00367-014-0357-3

Javanshir, R. J., Riley, G. W., Duppenbecker, S. J., & Abdullayev, N. (2015). Validation of lateral fluid flow in an overpressured sand-shale sequence during development of Azeri-Chirag-Gunashli oil field and Shah Deniz gas field: South Caspian Basin, Azerbaijan. *Marine and Petroleum Geology*, *59*, 593–610. https://doi.org/10.1016/j.marpetgeo.2014.07.019

Kirkham, C., Cartwright, J., Hermanrud, C., & Jebsen, C. (2017a). The genesis of mud volcano conduits through thick evaporite sequences. *Basin Research*, *30*(2), 217–236. https://doi.org/10.1111/bre.12250

Kirkham, C., Cartwright, J., Hermanrud, C., & Jebsen, C. (2017b). The spatial, temporal and volumetric analysis of a large mud volcano province within the Eastern Mediterranean. *Marine and Petroleum Geology*, *81*, 1–16. https://doi.org/10.1016/j.marpetgeo.2016.12.026

Kopf, A. J. (2002). Significance of mud volcanism. *Reviews of Geophysics*, *40*(2), 1005. https://doi.org/10.1029/2000RG000093

Lamontagne, R. A., Swinnerton, J. W., Linnenbom, V. J., & Smith, W. D. (1973). Methane concentrations in various marine environments and atmospheric methane centration of 1.24 ppm for the atmosphere above number of stranded fjords and lakes Str m, decomposition of organic waters the mechanism of methane production appears to. *Journal of Geophysical Research*, *78*(24), 5317–5324. https://doi.org/10.1029/JC078i024p05317

Lin, W., Yamamoto, K., Ito, H., Masago, H., & Kawamura, Y. (2008). Estimation of minimum principal stress from an extended leak-off test onboard the Chikyu drilling vessel and suggestions for future test procedures. *Scientific Drilling*, *6*, 43–47. https://doi.org/10.2204/lodp.sd.6.06.2008

Mazzini, A., & Etiope, G. (2017). Mud volcanism: An updated review. *Earth-Science Reviews*, *168*, 81–112. https://doi.org/10.1016/j.earscirev.2017.03.001

Mazzini, A., Etiope, G., & Svensen, H. (2012). A new hydrothermal scenario for the 2006 Lusi eruption, Indonesia. Insights from gas geochemistry. *Earth and Planetary Science Letters*, *317-318*(May 2006), 305–318. https://doi.org/10.1016/j.epsl.2011.11.016

Mazzini, A., Svensen, H., Akhmanov, G. G., Aloisi, G., Planke, S., Malthe-Sørenssen, A., & Istadi, B. (2007). Triggering and dynamic evolution of the LUSI mud volcano, Indonesia. *Earth and Planetary Science Letters*, *261*(3–4), 375–388. https://doi.org/10.1016/j.epsl.2007.07.001

Milkov, A. V. (2000). Worldwide distribution of submarine mud volcanoes and associated gas hydrates. *Marine Geology*, *167*(1–2), 29–42. https://doi.org/10.1016/S0025-3227(00)00022-0

Morley, C. K., King, R., Hillis, R., Tingay, M., & Backe, G. (2011). Earth-science reviews deepwater fold and thrust belt classi fi cation, tectonics, structure and hydrocarbon prospectivity: A review. *Earth Science Reviews*, *104*(1–3), 41–91. https://doi.org/10.1016/j.earscirev.2010.09.010

Mosar, J., Kangarli, T., Bochud, M., Glasmacher, U. A., Rast, A., Brunet, M.-F., & Sosson, M. (2010). Cenozoic-recent tectonics and uplift in the greater Caucasus: a perspective from Azerbaijan. *Geological Society, London, Special Publications*, *340*(1), 261–280. https://doi.org/10.1144/SP340.12

Nadirov, R. S., Bagirov, E., Tagiyev, M., & Lerche, I. (1997). Flexural plate subsidence, sedimentation rates, and structural development of the super-deep South Caspian Basin. *Marine and Petroleum Geology*, *14*(4), 383–400. https://doi.org/10.1016/S0264-8172(96)00054-2

Nely, G. (1986). 8. La méthode de sismique réflexion. In *Méthodes Géophysiques (Vol. 2)* (pp. 147–244). Editions TECHNIP.

Obradors-Prats, J., Rouainia, M., Aplin, A. C., & Crook, A. J. L. (2017). Assessing the implications of tectonic compaction on pore pressure using a coupled geomechanical approach. *Marine and Petroleum Geology*, *79*, 31–43. https://doi.org/10.1016/j.marpetgeo.2016.10.017

Oppo, D., Capozzi, R., Nigarov, A., & Esenov, P. (2014). Mud volcanism and fluid geochemistry in the Cheleken peninsula, western Turkmenistan. *Marine and Petroleum Geology*, *57*, 122–134. https://doi.org/10.1016/j.marpetgeo.2014.05.009

Osborne, M. J., & Swarbrick, R. E. (1997). Mechanisms for generating overpressure in sedimentary basins: A reevaluation 1. *AAPG Bulletin*, *6*(6), 1023–1041.

Pollastro, R. M. (1993). Considerations and applications of the illite/smectite geothermometer in hydrocarbon-bearing rocks of miocene to Mississippian age. *Clays and Clay Minerals*, *41*(2), 119–133. https://doi.org/10.1346/CCMN.1993.0410202

Popov, S. V., Rögl, F., Rozanov, A. Y., Steininger, F. F., Shcherba, I. G., & Kovac, M. (2004). Lithological-paleogeographic maps of para-tethys. CFS Courier Forschungsinstitut Senckenberg.

Ren, X., Zhao, Y., Deng, Q., Kang, J., Li, D., & Wang, D. (2016). A relation of hydraulic conductivity—Void ratio for soils based on Kozeny-carman equation. *Engineering Geology*, *213*, 89–97. https://doi.org/10.1016/j.enggeo.2016.08.017

Ricker, N. (1953). The form and laws of propagation of seismic wavelets. *Geophysics*, *18*(1), 10–40. https://doi.org/10.1190/1.1437843

Rietveld, H. M. (1969). A profile refinement method for nuclear and magnetic structures. *Journal of Applied Crystallography*, *2*(2), 65–71. https://doi.org/10.1107/S0021889869006558

Robein, E. (2010). *Seismic imaging. A review of the techniques, their principles, merits and limitations*. Houten, The Netherlands: EAGE Publications bv.

Roberts, K. S., Davies, R. J., & Stewart, S. A. (2010). Structure of exhumed mud volcano feeder complexes, Azerbaijan. *Basin Research*, *22*(4), 439–451. https://doi.org/10.1111/j.1365-2117.2009.00441.x

Ryzak, M., & Bieganowski, A. (2011). Methodological aspects of determining soil particle-size distribution using the laser diffraction method. *Journal of Plant Nutrition and Soil Science*, *174*(4), 624–633. https://doi.org/10.1002/jpln.201000255

Savage, H. M., & Brodsky, E. E. (2011). Collateral damage: Evolution with displacement of fracture distribution and secondary fault strands in fault damage zones. *Journal of Geophysical Research*, *116*, B03405. https://doi.org/10.1029/2010JB007665

Sibson, R. H. (2003). Brittle-failure controls on maximum sustainable overpressure in different tectonic regimes. *American Association of Petroleum Geologists Bulletin*, *87*(6), 901–908. https://doi.org/10.1306/01290300181

Stewart, S. A., & Davies, R. J. (2006). Structure and emplacement of mud volcano systems in the South Caspian Basin. *AAPG Bulletin*, *90*(5), 771–786. https://doi.org/10.1306/11220505045

Sultan, N., Cochonat, P., Canals, M., Cattaneo, A., Dennielou, B., Haflidason, H., et al. (2004). Triggering mechanisms of slope instability processes and sediment failures on continental margins: A geotechnical approach. *Marine Geology*, *213*(1–4), 291–321. https://doi.org/10.1016/j.margeo.2004.10.011

Sultan, N., De Gennaro, V., & Puech, A. (2012). Mechanical behaviour of gas-charged marine plastic sediments. *Géotechnique*, *62*(9), 751–766. https://doi.org/10.1680/geot.12.OG.002

Swarbrick, R. E., Osborne, M. J., & Yardley, G. S. (2002). Comparision of overpressure magnitude resulting from the main generating mechanisms generating mechanisms. *AAPG Memoir*, *76*, 1–12.

Terzaghi, K. (1943). *Theoretical soil mechanics*. New York: John Wiley and Sons Incorporated, Ed.

Tingay, M., Heidbach, O., Davies, R., & Swarbrick, R. (2008). Triggering of the Lusi mud eruption: Earthquake versus drilling initiation. *Geology*, *36*(8), 639–642. https://doi.org/10.1130/G24697A.1

Tingay, M., Manga, M., Rudolph, M. L., & Davies, R. (2017). An alternative review of facts, coincidences and past and future studies of the Lusi eruption. *Marine and Petroleum Geology*, *95*, 345–361. (December). https://doi.org/10.1016/j.marpetgeo.2017.12.031

Tingay, M. R. P., Rudolph, M. L., Manga, M., Davies, R. J., & Wang, C.-Y. (2015). Initiation of the Lusi mudflow disaster. *Nature Geoscience*, *8*(7), 493–494. https://doi.org/10.1038/ngeo2472

Wyllie, M. R. J., Gregory, A. R., & Gardner, G. H. F. (1958). An experimental investigation of factors affecting elastic wave velocities in porous media. *Geophysics*, *23*(3), 459–493. https://doi.org/10.1190/1.1438493

Zitter, T. (2004). Mud volcanism and fluid emissions in Eastern Mediterranean neotectonic zones. *Free University of Amsterdam*, *121*(07). https://doi.org/10.1017/S002221510700713X